

Optimal perturbations of gravitationally unstable, transient, boundary layers in porous media

Don Daniel*, Nils Tilton†, Amir Riaz‡

Abstract

We study gravitationally unstable, ‘transient’, diffusive boundary layers in porous media using modal and nonmodal stability methods. Using nonmodal stability theory, we demonstrate that both the onset of instabilities and the shape of optimal perturbations are highly sensitive to perturbation amplification measures and also the time at which the boundary layer is perturbed. This behavior is in contrast to traditional studies of steady or non-transient diffusive boundary layers where perturbation dynamics are independent of perturbation measure or time. We demonstrate that any analysis of transient layers produced through classical methods can result in physically unrealizable perturbation structures. To resolve the issue, we propose a non-modal stability procedure which additionally constrains the perturbation dynamics to physically admissible fields. The proposed procedure predicts that instabilities grow primarily due to unstable perturbations featuring much larger spanwise wavenumbers (modes) and smaller amplifications compared to perturbations predicted using classical methods. We validate our predictions using direct numerical simulations that emulate the onset of convection in physical systems.

1 Introduction

Gravitationally unstable, transient, solute boundary layers in porous media have been studied extensively due to their importance in carbon dioxide sequestration in porous, brine-saturated, subsurface aquifers. After injection in an aquifer, buoyant CO₂ rises and forms a horizontal layer beneath an impermeable caprock. With time, the CO₂ dissolves into the underlying brine and forms a downwardly growing diffusive boundary layer, as illustrated in figure 1. As CO₂ diffuses downwards, the solute boundary layer is naturally perturbed by local aquifer heterogeneities. Because the CO₂-rich brine in the boundary layer is denser than the underlying brine, a gravitational instability eventually causes perturbations to grow and form finger-like structures that break away from the boundary layer and convect CO₂ downwards into the aquifer. A clear understanding of the physical mechanisms and dominant perturbation structures that cause finger-formation is vital to modelling CO₂ sequestration. Furthermore, similar transient boundary layers occur in purely fluid media [1] and are important for heat transfer devices [2] and geophysical flows [3].

In comparison to classical Rayleigh-Bénard convection [4], the stability of transient diffusive boundary layers is complicated by the transient base-state that renders the linear stability operator non-autonomous. At small times when the boundary layer is beginning to form, perturbations to the layer are damped by stabilizing effects of diffusion. Eventually, a critical time for linear instability, $t = t_c$, is reached after which perturbations begin to grow. For small initial perturbations, linear mechanisms can dominate for considerable time beyond t_c [5, 6, 7, 8]. Within this linear regime, the flux of CO₂ into the brine, J , decreases monotonically. Eventually nonlinear mechanisms cause the flux of CO₂ to increase from that predicted by linear theory such that there is a turning point where $dJ/dt = 0$. Motivated by experimental studies [9], we define the time at which this turning point occurs as the onset time of nonlinear convection, $t = t_o$.

*dond@lanl.gov

†ntilton@mines.edu

‡ariaz@umd.edu, Department of Mechanical Engineering, University of Maryland, College Park, MD 20742, USA

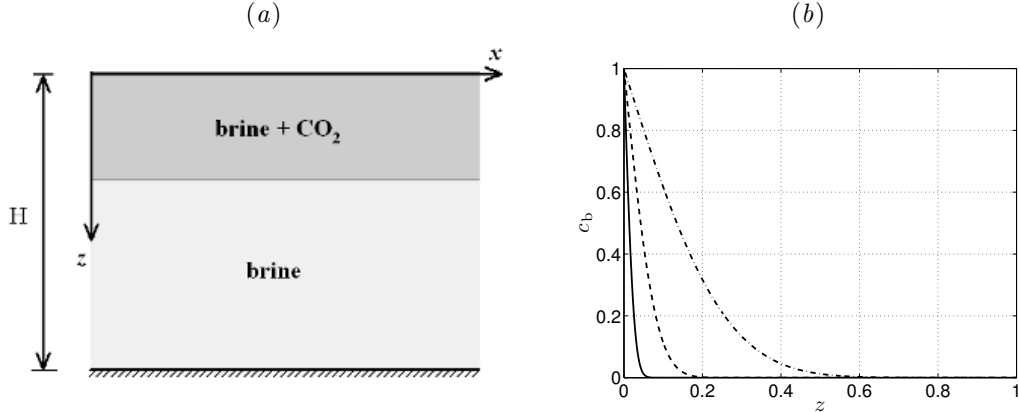


Figure 1: (a) Sketch, not to scale, of the geometry considered in this study. (b) Base-state (3) for $Ra = 500$ and $t = 0.1$ (solid line), $t = 1$ (dashed line), and $t = 10$ (dash-dotted line).

Various methods have been used to study the linear regime preceding onset of convection, for detailed review, see Refs. [8, 10, 11]. One approach invokes the quasi-steady-state-assumption (QSSA) and performs a modal analysis. The QSSA eigenmodes, however, are non-orthogonal, and there is potential for nonmodal growth [12]. Thus motivated, recent studies (for example, see Ref. [8]) use traditional nonmodal methods [13, 14, 12] to the nonautonomous linear initial value problem (IVP) to determine optimal perturbations with maximum amplification at a later time. However, in this study, we show that optimal perturbations predicted through such classical means cannot lead to onset of convection in finite time. Rather, onset of convection results from the growth of “suboptimal” perturbations localized within the diffusive boundary layer. To determine such perturbations, we propose a non-modal method based on an adjoint Lagrangian formulation.

This study is organized as follows. The governing equations are presented in §2. The classical optimization procedure, without application of the physical constraint, is described in §3. The classical optimization results are presented in §4. The proposed modifications to the classical optimization procedure and associated results are presented in §5. DNS results are reported in §6. The main findings are summarized in §7.

2 Geometry and governing equations

Due to the fundamental nature of the current study, we consider an isotropic, homogeneous, fluid-saturated porous medium of infinite horizontal extent in the x and y directions, and of finite depth H in the vertical z direction, see figure 1(a). This facilitates comparison with the previous nonmodal analysis of [8]. The analysis considered in the current study can be extended to anisotropic heterogeneous media. We define the vertical z direction as positive in the downward direction of gravity, g . The domain is bounded by an impermeable wall at $z = H$. The porous medium is characterized by its permeability, K , dispersivity, D , and porosity, ϕ , respectively. Initially, the brine is quiescent with zero CO_2 concentration, $c = 0$, and constant density, $\rho = \rho_0$. At time $t = 0$, saturated brine is supplied at $z = 0$ with a constant concentration $c = C_1$ and density ρ_1 . The fluid viscosity, μ , is assumed to be constant. The density difference $\Delta\rho = \rho_1 - \rho_0$ is assumed to be much less than ρ_0 , i.e. $\Delta\rho \ll \rho_0$.

Fluid flow and mass transport in the porous medium are governed by Darcy’s law and volume averaged forms of the continuity and advection-diffusion equations [15]. The governing equations are written in nondimensional form as,

$$\mathbf{v} + \nabla p - c\mathbf{e}_z = 0, \quad \nabla \cdot \mathbf{v} = 0, \quad \frac{\partial c}{\partial t} + \mathbf{v} \cdot \nabla c - \frac{1}{Ra} \nabla^2 c = 0, \quad (1)$$

using the characteristic length $L = H$, time $T = \phi H/U$, buoyancy velocity $U = K\Delta\rho g/\mu$, pressure

$P = \Delta\rho gH$, and concentration $C = C_1$. The dimensionless equations (1) have been obtained using the Boussinesq approximation and a linear fluid density profile, $\rho = \rho_0 + \Delta\rho(c/C_1)$. The Rayleigh number is defined as $Ra = UH/(\phi D)$. The symbol $\mathbf{v} = [u, v, w]$ is the nondimensional velocity vector, c is the nondimensional concentration and p is the nondimensional pressure obtained from the dimensional pressure \hat{p} through the relation $p = (\hat{p} - \rho_0 g z)/P$. The symbol \mathbf{e}_z is the unit vector in the z direction. Equations (1) must satisfy the following boundary conditions,

$$c\Big|_{z=0} = 1, \quad \frac{\partial c}{\partial z}\Big|_{z=1} = 0, \quad w\Big|_{z=0} = w\Big|_{z=1} = 0, \quad t \geq 0. \quad (2)$$

Equations (1) admit the transient base state,

$$\mathbf{v}_b = \mathbf{0}, \quad c_b(z, t) = 1 - \frac{4}{\pi} \sum_{n=1}^{\infty} \frac{1}{2n-1} \sin\left[\left(n - \frac{1}{2}\right) \pi z\right] \exp\left[-\left(n - \frac{1}{2}\right)^2 \frac{\pi^2 t}{Ra}\right], \quad (3)$$

We study the linear stability of base-state (3) with respect to small wavelike perturbations of the form,

$$\tilde{c} = \hat{c}(z, t)e^{i(\alpha x + \beta y)}, \quad \tilde{\mathbf{v}} = \hat{\mathbf{v}}(z, t)e^{i(\alpha x + \beta y)}, \quad \tilde{p} = \hat{p}(z, t)e^{i(\alpha x + \beta y)}, \quad (4)$$

where $i = \sqrt{-1}$, α and β are wavenumbers in the x and y directions respectively, and $\hat{c}(z, t)$, $\hat{\mathbf{v}}(z, t)$ and $\hat{p}(z, t)$ are time-dependent perturbation profiles in the z direction. Following the standard procedure [see 5], the linear stability problem can be written as the following initial value problem for \hat{c} and \hat{w} ,

$$\frac{\partial \hat{c}}{\partial t} + \hat{w} \frac{\partial c_b}{\partial z} - \frac{1}{Ra} \mathcal{D} \hat{c} = 0, \quad \mathcal{D} \hat{w} + k^2 \hat{c} = 0, \quad (5)$$

$$\hat{c}\Big|_{z=0} = 0, \quad \frac{\partial \hat{c}}{\partial z}\Big|_{z=1} = 0, \quad \hat{w}\Big|_{z=0} = \hat{w}\Big|_{z=1} = 0, \quad (6)$$

where $\mathcal{D} = \partial^2/\partial z^2 - k^2$ and $k = \sqrt{\alpha^2 + \beta^2}$. Because the base-state is transient, the boundary layer is sensitive to the time at which it is perturbed. We assume the layer is perturbed at time $t = t_p$ with the following initial perturbation profiles,

$$\hat{c}\Big|_{t=t_p} = c_p(z), \quad \hat{w}\Big|_{t=t_p} = w_p(z), \quad (7)$$

where c_p and w_p must satisfy equations (5)–(6).

3 Classical Optimization

The initial perturbation profiles, c_p and w_p , are determined so that the perturbation amplification is maximized at some prescribed final time $t = t_f$. Previous studies [16, 17] have observed that the perturbation amplification is sensitive to the perturbation flow field used to measure the perturbation magnitude. To investigate how different measures of perturbation magnitude influence nonmodal results, we define the perturbation magnitude at time t as,

$$E(t) = \int_0^1 [A_1 \hat{c}(z, t)^2 + A_2 \hat{w}(z, t)^2 + A_3 \hat{u}(z, t)^2] dz, \quad (8)$$

where A_1, A_2 and A_3 are constants to be defined shortly. We introduce the following measures of perturbation amplification, $\Phi(t)$,

$$\Phi_c(t) = \left[\frac{E(t)}{E(t_p)} \right]^{\frac{1}{2}}, \quad A_1 = 1, \quad A_2 = A_3 = 0, \quad (9a)$$

$$\Phi_w(t) = \left[\frac{E(t)}{E(t_p)} \right]^{\frac{1}{2}}, \quad A_2 = 1, \quad A_1 = A_3 = 0, \quad (9b)$$

$$\Phi_e(t) = \left[\frac{E(t)}{E(t_p)} \right]^{\frac{1}{2}}, \quad A_1 = A_2 = A_3 = 1. \quad (9c)$$

Most previous studies of transient boundary layers measure amplification with respect to the perturbation's concentration field, Φ_c [18, 16, 19, 20, 8], or the vertical velocity field, Φ_w [21, 22, 23, 16]. In addition, we introduce Φ_e as a measure of perturbation energy that includes both the velocity and concentration fields. We optimize $\Phi(t_f)$ using an adjoint procedure described by [17] in which $E(t_f)$ is maximized subject to the constraint that $E(t_p) = 1$. For this purpose, we define the Lagrangian,

$$\begin{aligned} \mathcal{L}(\hat{c}, c^*, \hat{w}, w^*, \hat{u}, s) &= E(t_f) - s[E(t_p) - 1] - \int_{t_p}^{t_f} \int_0^1 w^* (\mathcal{D}\hat{w} + k^2\hat{c}) \, dz \, dt \\ &\quad - \int_{t_p}^{t_f} \int_0^1 c^* \left(\frac{\partial \hat{c}}{\partial t} - \frac{1}{Ra} \mathcal{D}\hat{c} + \hat{w} \frac{\partial c_b}{\partial z} \right) \, dz \, dt, \end{aligned} \quad (10)$$

where s is a scalar Lagrange multiplier and the adjoint variables $c^*(z, t)$ and $w^*(z, t)$ are Lagrange multipliers dependent on z and t . The double integrals on the right-hand-side of (10) assure satisfaction of the governing IVP (5)–(7). To obtain first-order optimality conditions, the variational of the Lagrangian, $\delta\mathcal{L}$, is set to zero. Integrating by parts, $\delta\mathcal{L}$ can be written as,

$$\begin{aligned} \delta\mathcal{L} &= \int_0^1 \left[2(A_1\hat{c}\delta\hat{c} + A_2\hat{w}\delta\hat{w} + A_3\hat{u}\delta\hat{u}) - c^*\delta\hat{c} \right]_{t=t_f} \, dz \\ &\quad - \int_0^1 \left[2s(A_1\hat{c}\delta\hat{c} + A_2\hat{w}\delta\hat{w} + A_3\hat{u}\delta\hat{u}) - c^*\delta\hat{c} \right]_{t=t_p} \, dz \\ &\quad - \int_{t_p}^{t_f} \int_0^1 \left[\delta\hat{c} \left(-\frac{\partial c^*}{\partial t} - \frac{1}{Ra} \mathcal{D}c^* + k^2w^* \right) + \delta\hat{w} \left(\mathcal{D}w^* + \frac{\partial c_b}{\partial z} c^* \right) \right] \, dz \, dt \\ &\quad + \int_{t_p}^{t_f} \left[\frac{1}{Ra} \left(c^* \frac{\partial \delta\hat{c}}{\partial z} - \delta\hat{c} \frac{\partial c^*}{\partial z} \right) - w^* \frac{\partial \delta\hat{w}}{\partial z} + \delta\hat{w} \frac{\partial w^*}{\partial z} \right]_{z=0}^{z=1} \, dt = 0. \end{aligned} \quad (11)$$

The optimality conditions are met when c^* and w^* satisfy the following adjoint problem,

$$-\frac{\partial c^*}{\partial t} - \frac{1}{Ra} \mathcal{D}c^* + k^2w^* = 0, \quad \mathcal{D}w^* = -\frac{\partial c_b}{\partial z} c^*, \quad (12)$$

$$c^* \Big|_{z=0} = 0, \quad \frac{\partial c^*}{\partial z} \Big|_{z=1} = 0, \quad w^* \Big|_{z=0} = w^* \Big|_{z=1} = 0, \quad (13)$$

along with the following coupling conditions between the adjoint and physical variables,

$$2(A_1\hat{c}\delta\hat{c} + A_2\hat{w}\delta\hat{w} + A_3\hat{u}\delta\hat{u}) \Big|_{t=t_f} = c^*\delta\hat{c} \Big|_{t=t_f}, \quad (14)$$

$$2s(A_1\hat{c}\delta\hat{c} + A_2\hat{w}\delta\hat{w} + A_3\hat{u}\delta\hat{u}) \Big|_{t=t_p} = c^*\delta\hat{c} \Big|_{t=t_p}. \quad (15)$$

The optimal initial perturbations are found using an iterative procedure. Given an initial guess for c_p and w_p , we integrate the IVP (5)–(7) forward in time to $t = t_f$. We then apply the condition (14) to obtain a final condition for the adjoint IVP (12)–(13). The adjoint IVP is then integrated backwards in time to $t = t_p$. We then use condition (15) to obtain improved initial profiles c_p and w_p . This procedure is repeated until satisfaction of the convergence criteria, $\|c_p^n - c_p^{n-1}\|_\infty / \|c_p^{n-1}\|_\infty \leq 10^{-4}$, where n is the iteration number. The iterative procedure is insensitive to the initial guess; however, the number of iterations is reduced using $c_p^0 = \xi \exp(-\xi^2)$ where $\xi = z\sqrt{Ra/(4t)}$. The IVPs are solved using standard second-order finite-difference methods.

The application of the coupling conditions (14)–(15) depends on the definition of the perturbation amplification. When maximizing Φ_c , conditions (14)–(15) are satisfied for,

$$2\hat{c}\Big|_{t=t_f} = c^*\Big|_{t=t_f}, \quad 2s\hat{c}\Big|_{t=t_p} = c^*\Big|_{t=t_p}. \quad (16)$$

The derivation of (16) is described in Ref. [17]. When maximizing Φ_w or Φ_e , however, the application of the coupling conditions is less straightforward than in the case of [17] because in the current study, the momentum equation lacks a temporal derivative. For those cases, we found it necessary to replace the Neumann boundary conditions for \hat{c} and c^* at the lower wall with the following Dirichlet condition,

$$\hat{c}\Big|_{z=1} = c^*\Big|_{z=1} = 0. \quad (17)$$

Consequently, when maximizing Φ_w , coupling conditions (14)–(15) are satisfied for,

$$-2k^2\hat{w}\Big|_{t=t_f} = \mathcal{D}c^*\Big|_{t=t_f}, \quad -2k^2s\hat{w}\Big|_{t=t_p} = \mathcal{D}c^*\Big|_{t=t_p}. \quad (18)$$

When maximizing Φ_e , conditions (14)–(15) are satisfied for,

$$\left(k^2\frac{\partial^2}{\partial z^2} - k^4 - \mathcal{D}^2\right)\hat{w}\Big|_{t=t_f} = \frac{k^2}{2}\mathcal{D}c^*\Big|_{t=t_f}, \quad (19)$$

$$s\left(k^2\frac{\partial^2}{\partial z^2} - k^4 - \mathcal{D}^2\right)\hat{w}\Big|_{t=t_p} = \frac{k^2}{2}\mathcal{D}c^*\Big|_{t=t_p}. \quad (20)$$

For the parameter space (t_p, t_f, Ra, k) considered in the current study, the Dirichlet condition (17) is valid because the optimal perturbations are concentrated near $z = 0$ and decay to zero outside the boundary layer such that they are not influenced by the lower wall [8, 24]. We validated our results by directly optimizing the IVP (5)–(7), subject to the standard boundary conditions (6), using MATLAB routines. The adjoint-based method shows excellent agreement with direct optimization but is an order-of-magnitude faster.

4 Classical optimization results

Previously, Ref. [8] reported optimal perturbations that maximize Φ_c for a fixed initial perturbation time, t_p . We extend their work in the following manner. First, we explore how the amplification measure (9) affects the optimization results. Second, we investigate the role of the initial perturbation time. Third, we study the influence of the final time on the initial optimal profiles. Fourth, we compare the optimal perturbations with quasi-steady eigenmodes. Finally, in §5, we assess the relevance of the optimal perturbations to physical experiments.

4.1 Effect of amplification measure

Figure 2 presents optimization results for $Ra = 500$ and $t_p = 0.01$ when maximizing Φ_c , Φ_w , and Φ_e . The Rayleigh number is set to a typical value for CO₂ sequestration [25]. The initial perturbation time is chosen to be one order-of-magnitude smaller than the critical time for instability, t_c , where the critical time is the time at which $d\Phi/dt = 0$, after which Φ begins to increase. The critical time depends on the initial condition and choice of the amplification measure; however, previous analyses find the minimum critical time is on the order of $t_c \sim O(0.1)$ for $Ra = 500$ [5, 26, 24]. Panel (a) illustrates optimal isocontours of Φ_c (solid lines), Φ_w (dashed lines), and Φ_e (dash-dotted lines) in the (k, t_f) plane. The three amplification measures produce qualitatively similar behavior. The isocontours for Φ_c and Φ_e are visually indistinguishable. For much of the (k, t_f) plane, Φ_w is marginally larger than Φ_c or Φ_e .

We define the dominant wavenumber, k_{\max} , as the wavenumber for which the amplification is maximized at t_f ,

$$\Phi_{\max}(t_f) = \sup_{0 \leq k < \infty} \Phi(t_f, k). \quad (21)$$

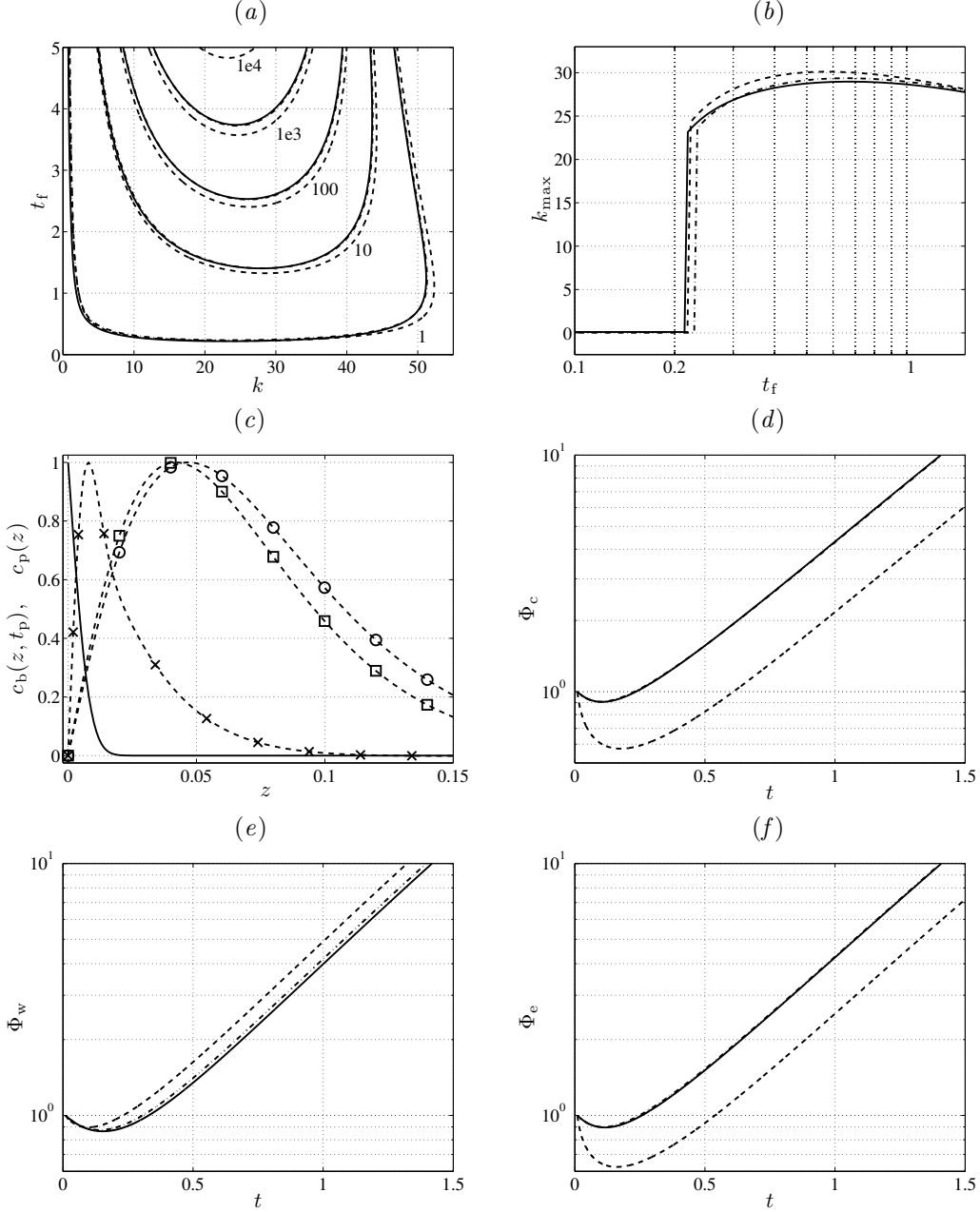


Figure 2: Optimization results for $Ra = 500$ and $t_p = 0.01$ when maximizing Φ_c , Φ_w and Φ_e , respectively. (a) Isocontours of Φ_c (solid line), Φ_w (dashed line), and Φ_e (dash-dotted line) in the (k, t_f) plane. The Φ_c and Φ_e lines are visually indistinguishable. (b) Dominant wavenumbers, k_{\max} , vs. t_f , when maximizing Φ_c (solid line), Φ_w (dashed line), and Φ_e (dash-dotted line). A log scale has been used for t_f . (c) The optimal c_p profiles when maximizing Φ_c (circles), Φ_w (crosses), and Φ_e (squares) for $k = 30$ and $t_f = 5$. The base state $c_b(z, t_p)$ is shown as a solid line. (d)–(f) Amplifications Φ_c , Φ_w , and Φ_e vs. t when integrating the forward IVP (5)–(7) in time using the optimal initial c_p profiles shown in panel (c), that maximize Φ_c (solid line), Φ_w (dashed line), and Φ_e (dash-dotted line).

Figure 2(b) illustrates the dominant wavenumbers that maximize Φ_c (solid line), Φ_w (dashed line), and Φ_e (dash-dotted line) for the final times $0.1 \leq t_f \leq 2$. The dominant wavenumbers for the three amplification measures are qualitatively similar. When $t_f \leq 0.21$, the dominant wavenumbers are zero. When $t_f > 0.21$, the dominant wavenumbers jump discontinuously to values around $k_{\max} \approx 25$. The dominant zero-wavenumber perturbations were not reported by [8] because they considered late values of t_f for which k_{\max} is non-zero. When comparing results of [8] with the current study, one must note that [8] nondimensionalized the problem with a diffusive time scale, while we use an advective time scale. Consequently, the nondimensional times, t , in this study are related to those of [8], $t^{(R)}$, through the relation $t^{(R)} = t/Ra$.

Though maximizing different perturbation fields produces similar dominant wavenumbers, k_{\max} , the corresponding optimal initial profiles, c_p and w_p , are sensitive to the amplification measure. Figure 2(c) illustrates the optimal c_p profiles that maximize Φ_c (circles), Φ_w (crosses), and Φ_e (squares) at $t_f = 5$ for $k = 30$. For visualization, the profiles have been scaled so $\|c_p\|_\infty = 1$. The solid line shows the base-state at $t_p = 0.01$. Figure 2(c) shows results for $0 \leq z \leq 0.15$ because the profiles are concentrated near $z = 0$ and decay to zero before interacting with the lower wall $z = 1$. The profiles for Φ_e and Φ_c have maxima occurring around $z = 0.05$, while the profile for Φ_w has a maximum occurring around $z = 0.01$.

Figure 2(d) illustrates the temporal evolution of Φ_c when the forward IVP (5)–(7) is integrated from $t_p = 0.01$ to $t = 2$ using the three initial c_p profiles illustrated in figure 2(c). The c_p profiles that maximize Φ_c (solid line) and Φ_e (dash-dotted line) produce indistinguishable results in figure 2(d). The c_p profile that maximizes Φ_w (dashed line), however, produces much lower values of Φ_c . This suggests that maximization of Φ_w occurs at the expense of Φ_c . Figure 2(e) illustrates the corresponding results for the evolution of Φ_w . The c_p profiles that maximize Φ_c (solid line) and Φ_e (dash-dotted line) produce nearly indistinguishable results, while the profile that maximizes Φ_w (dashed line) produces marginally larger Φ_w . Finally, figure 2(f) illustrates the corresponding results for the evolution of Φ_e . The initial profiles that maximize Φ_c and Φ_e again produce indistinguishable results. This indicates that maximizing the perturbation’s concentration field naturally maximizes Φ_e , while maximizing Φ_w does so at the expense of Φ_c and Φ_e . Because Φ_c naturally maximizes Φ_e , hereinafter we focus on maximizing Φ_c . We choose Φ_c over Φ_e because the application of the coupling conditions (14)–(15) is much simpler for Φ_c .

4.2 Sensitivity to wavenumber k

Figure 3(a) illustrates the optimal amplifications Φ_c versus t_f for $t_p = 0.01$, and $k = 0$ (circles), $k = 10$ (crosses), $k = 25$ (squares), and $k = 40$ (diamonds). For small final times, $t_f < 0.1$, all perturbations decay; however, the $k = 25$ perturbations are more damped than the $k = 0$ and $k = 10$ perturbations. Note that the $k = 0$ perturbations have a small constant damping rate. This occurs because the IVP (5)–(7) for $k = 0$ reduces to

$$\frac{\partial \hat{c}}{\partial t} - \frac{1}{Ra} \frac{\partial^2 \hat{c}}{\partial z^2} = 0, \quad \hat{w} = 0. \quad (22)$$

Equation (22) can be solved analytically to show that the optimal perturbation is given by

$$\hat{c} = \sin(\pi z/2) \exp(-\pi^2 Ra^{-1} t/4).$$

In contrast to the $k = 0$ perturbations, finite wavenumber perturbations do not have constant growth rates. The $k = 25$ perturbations begin to grow around $t_f = 0.1$ and eventually overtake the $k = 10$ and $k = 0$ perturbations. This explains the discontinuous jump in the dominant wavenumbers from $k_{\max} = 0$ to $k_{\max} \approx 25$ illustrated in figure 2(b). The $k = 40$ perturbations experience greater damping, and consequently, never overtake the $k = 25$ perturbations.

Figure 3(b) illustrates the base state, $c_b(z, t_f)$ (solid line), and optimal profiles, $\hat{c}(z, t_f)$, at $t_f = 0.21$ for $k = 0$ (circles), $k = 10$ (crosses), $k = 20$ (squares), and $k = 30$ (diamonds). The final time is chosen to be near to the discontinuous jump in k_{\max} illustrated in figure 2(b). The optimal profile for $k = 0$ has a maximum at the lower boundary at $z = 1$, while the profiles for $k = 10, 20$, and 30 have maxima near $z = 0$. With increasing k , the optimal profiles become increasingly concentrated within the boundary layer.

The results for Φ_c and c_p illustrated in figure 3 can be explained physically by examining the competing effects of the stabilizing diffusive term, $\mathcal{D}\hat{c}/Ra$, and the destabilizing convective term, $\hat{w}\partial c_b/\partial z$,

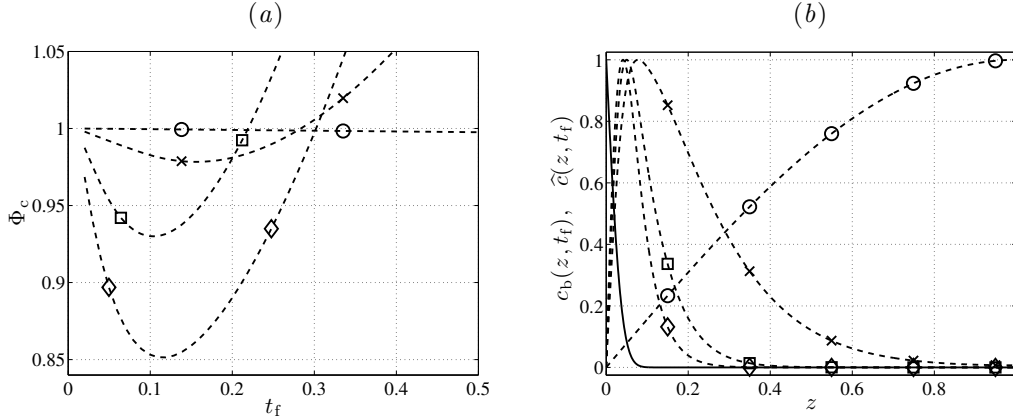


Figure 3: Dominant perturbations for $Ra = 500$ and $t_p = 0.01$. (a) Φ_c vs. t_f , for $k = 0$ (circles), $k = 10$ (crosses), $k = 25$ (squares), and $k = 40$ (diamonds). (b) $c_b(z, t_f)$ (solid line) and $\hat{c}(z, t_f)$ for $t_f = 0.21$, and $k = 0$ (circles), $k = 10$ (crosses), $k = 20$ (squares), and $k = 30$ (diamonds).

in equation (5). At small times, $t \ll t_c$, the convective term $\hat{w}\partial c_b/\partial z$ has only a small effect because $\partial c_b/\partial z$ is nonzero only within the thin boundary layer where \hat{w} necessarily tends to zero due to the no-penetration condition at $z = 0$. This explains why the boundary layer is stable at small times. The dominant wavenumber is initially zero because finite wavenumber perturbations have additional damping due to the transverse diffusive term $(k^2/Ra)\hat{c}$ in equation (5). At later times, the growing boundary layer increases the influence of the destabilizing term $\hat{w}\partial c_b/\partial z$ such that non-zero wavenumber perturbations become unstable. This explains why dominant perturbations at late times tend to be increasingly concentrated in the boundary layer.

4.3 Sensitivity to initial perturbation time t_p

Due to the transient nature of the base-state, the optimal perturbations also depend on the time, t_p , at which the boundary layer is perturbed. Figure 4 explores the sensitivity of the optimal amplifications Φ_c to the initial perturbation time t_p for $Ra=500$. Panel (a) illustrates Φ_c versus t_f for $k = 30$ and $t_p = 0.001$ (solid line), $t_p = 0.1$ (dashed line), and $t_p = 0.5$ (dash-dotted line). Perturbations originating at $t_p = 0.001$ have a long initial damping period and consequently have smaller amplifications than perturbations originating at $t_p = 0.1$. Perturbations originating at the late time $t_p = 0.5$ experience no damping, but have smaller amplifications than perturbations originating at $t_p = 0.001$ and $t_p = 0.1$ because those perturbations begin growing much earlier. At later times, $t_f > 0.5$, the three curves have identical slopes, indicating that the perturbations have identical temporal growth rates. Figure 4(b) illustrates isocontours of Φ_c in the (k, t_f) parameter plane for $t_p = 0.001$ (solid line), $t_p = 0.1$ (dashed line), and $t_p = 0.5$ (dash-dotted line). As expected, perturbations originating at $t_p = 0.1$ produce larger amplifications. The horizontal dash-dotted line indicates that perturbations originating at $t_p = 0.5$ grow immediately for $2 < k < 56$.

Figures 4(a) and 4(b) suggest that there exists an optimal initial perturbation time, t_p^o , that maximizes Φ_c . Perturbations originating prior to t_p^o cannot outgrow the optimal perturbation originating at t_p^o due to the initial damping period. From figure 4(a), we expect t_p^o to occur near the critical time, $t = t_c$, because this minimizes the damping period. Note that for $Ra = 500$, [24] report that the minimum critical time is $t_c \approx 0.096$. The notion of an optimal initial perturbation time may appear counterintuitive because in physical systems the boundary layer is continuously perturbed beginning at $t_p = 0$. Within the framework of a linear stability analysis, however, the response to this continuous forcing can be expressed as the infinite sum of many impulse responses to forcing at discrete initial times, t_p . The optimal perturbation originating at t_p^o gives a theoretical upper bound for the amplification.

Figure 4(c) illustrates the normalized amplifications, $\Phi_c/\|\Phi_c\|_\infty$, versus t_p for $t_f = 1$, and $k = 10$ (solid

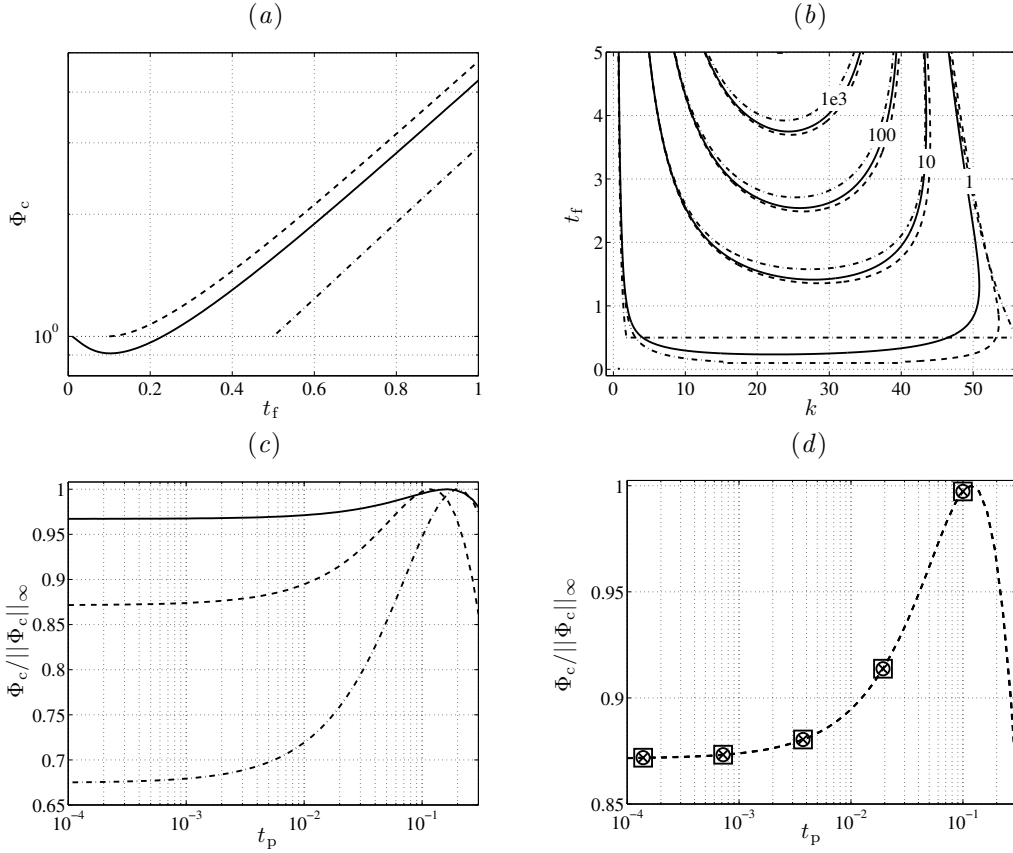


Figure 4: Effect of initial perturbation time for $Ra = 500$. (a) Φ_c vs. t_f for $k = 30$, and $t_p = 0.001$ (solid line), $t_p = 0.1$ (dashed line), and $t_p = 0.5$ (dash-dotted line). (b) Isocontours of Φ_c in the (k, t_f) plane for $t_p = 0.001$ (solid line), $t_p = 0.1$ (dashed line), and $t_p = 0.5$ (dash-dotted line). (c) $\Phi_c / \|\Phi_c\|_\infty$, vs. t_p for $t_f = 1$, and $k = 10$ (solid line), $k = 30$ (dashed line), $k = 50$ (dash-dotted line). (d) $\Phi_c / \|\Phi_c\|_\infty$ vs. t_p for $k = 30$ and $t_f = 1$ (circles), $t_f = 2$ (crosses), and $t_f = 3$ (squares).

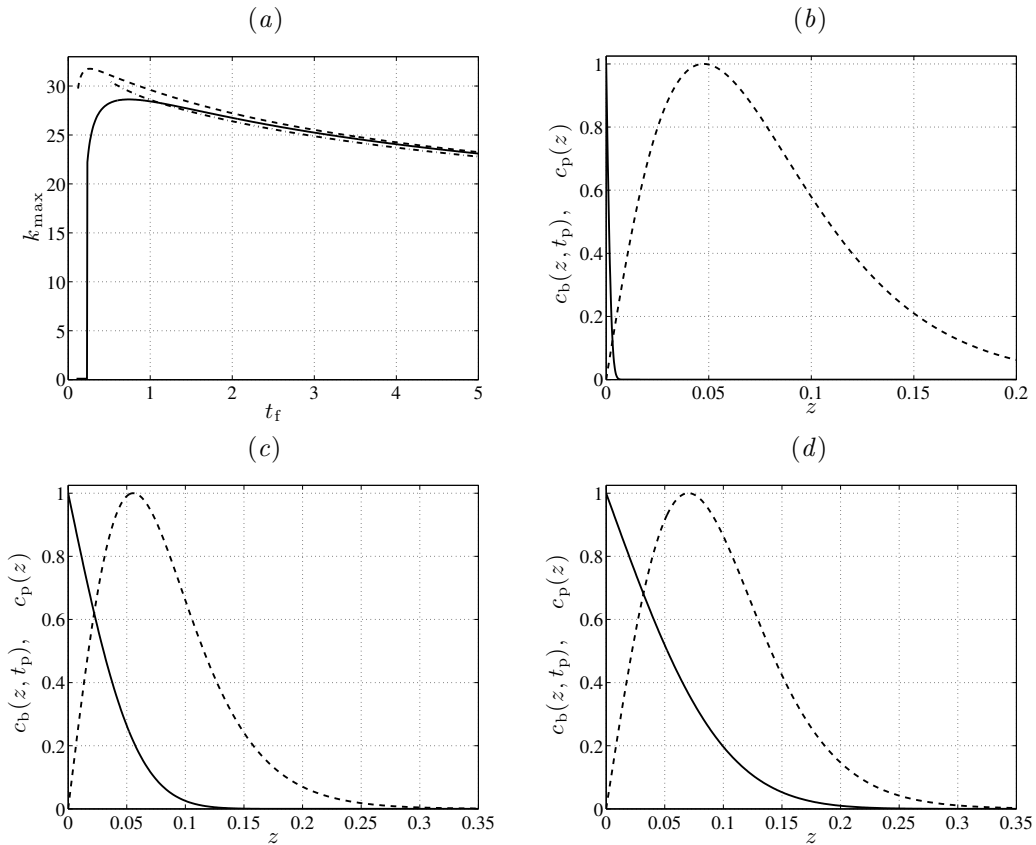


Figure 5: (a) Dominant wavenumbers, k_{\max} vs. t_f for $t_p = 0.001$ (solid line), $t_p = 0.1$ (dashed line), and $t_p = 0.5$ (dash-dotted line). (b) Base-state, c_b (solid line), and optimal c_p profiles (dashed line) for $t_p = 0.001$, $t_f = 5$, and $k = 30$. (c) Same as panel (b) for $t_p = 0.5$. (d) Same as panel (b) for $t_p = 1.5$. With increasing t_p , the c_p profiles become increasingly concentrated in the boundary layer.

line), $k = 30$ (dashed line), and $k = 50$ (dash-dotted line). The amplifications have been normalized with respect to their maximum values to facilitate comparison between the results for different wavenumbers. As $t_p \rightarrow 0$, the amplifications asymptote to constant values. With increasing t_p , the amplifications attain maxima near $t_p = t_c$ and then decrease. We observe stronger sensitivity of Φ_c to t_p with increasing wavenumber. This behavior is similar to that observed in figure 3(a) for the sensitivity of Φ_c to the final time t_f . The increasing sensitivity of Φ_c to both t_p and t_f at higher wavenumbers is likely due to the increase in transverse diffusive damping as noted in the previous section. Figure 4(d) illustrates $\Phi_c/\|\Phi_c\|_\infty$ versus t_p for $k = 30$ and $t_f = 1$ (circles), $t_f = 2$ (crosses), and $t_f = 3$ (squares). The results for different t_f are indistinguishable from each other. This occurs because, as demonstrated in figure 4(a), the perturbations have identical growth rates for $t_f > 1$.

Figure 5(a) illustrates the temporal evolution of the dominant wavenumbers, k_{\max} , when $t_p = 0.001$, (solid line), $t_p = 0.1$ (dashed line), and $t_p = 0.5$ (dash-dotted line). As expected from the discussion in §4.2, the dominant wavenumbers are initially zero when $t_p = 0.001$. When $t_p = 0.1$, however, the dominant wavenumber is initially $k_{\max} = 29.74$ for $t_f = 0.12$ and reaches a maximum at $t_f = 0.26$ after which it decays monotonically. When $t_p = 0.5$, k_{\max} decreases monotonically with t_f . Previously, [8] only reported cases with a monotonic decay of k_{\max} with t_f . Figures 5(b)–5(d) illustrate the base state (solid lines) and optimal c_p profiles (dashed lines), for $t_p = 0.001$ (panel b), $t_p = 0.5$ (panel c), and $t_p = 1.5$ (panel d) for $Ra = 500$, $k = 30$, and $t_f = 5$. As expected from the discussion in §4.2, the optimal profiles become increasingly concentrated within the boundary layer with increasing t_p due to the destabilizing convective term.

To explore the optimal initial perturbation time, we repeat the optimization procedure for a wide range of wavenumbers, initial times, and final times. Figure 6(a) illustrates the optimal amplifications Φ_c for $t_f = 1$, $Ra = 500$, $10 \leq k \leq 50$, and $0.01 \leq t_p \leq 0.5$. We define the maximum amplification, i.e. the peak of the Φ_c surface in figure 6(a), as

$$\Phi_c^\circ(t_f) = \sup_{\substack{0 \leq k < \infty \\ 0 < t_p < t_f}} \{\Phi_c(t_f, k, t_p)\}, \quad (23)$$

and the optimal point (k°, t_p°) as the location in the (k, t_p) plane where $\Phi = \Phi_c^\circ$. To explore the dependence of the optimal point on t_f and Ra , we compute $(\Phi_c^\circ, k^\circ, t_p^\circ)$ for $500 \leq Ra \leq 1000$ and $1 \leq t_f \leq 8$. Figure 6 demonstrates that the results collapse to three curves by plotting Φ_c° (panel b), k°/Ra (panel c), and $t_p^\circ Ra$ (panel d) as functions of $t_f Ra$. This collapse occurs because the optimal perturbations are concentrated near $z = 0$ and do not interact with the lower boundary at $z = 1$. Consequently, the Rayleigh number dependence may be scaled out of the governing equations (1)–(2) by approximating the vertical depth as infinite, $H \rightarrow \infty$, and nondimensionalizing the problem with respect to the characteristic length $L = \phi D/U$, and time, $T = \phi L/U$. From figure 6, we obtain the following relationships,

$$\log \Phi_c^\circ = -4.458 \times 10^{-8} (t_f Ra)^2 + 0.001721 t_f Ra - 0.05739, \quad (24)$$

$$k^\circ = Ra [0.1152 - 0.02023 \log(t_f Ra)], \quad (25)$$

$$t_p^\circ = 6.364 \times 10^{-4} t_f + 58.00/Ra, \quad (26)$$

For convenience, we also present relations (25) and (26) in dimensional form,

$$k^* = \frac{U}{\phi D} \left[0.1152 - 0.02023 \log \left(\frac{t_f^* U^2}{\phi^2 D} \right) \right], \quad (27)$$

$$t_p^* = 6.364 \times 10^{-4} t_f^* + 58.00 \frac{\phi^2 D}{U^2}, \quad (28)$$

where k^* , t_p^* , and t_f^* are the optimal wavenumber, initial time, and final time in dimensional form. Recall from §2 that $U = K \Delta \rho g / \mu$. These relations demonstrate that the optimal wavenumber and initial time are independent of the aquifer depth H . Note that when $t_f Ra < 1500$, relations (24) and (25) continue to provide accurate estimates, while relation (26) deviates significantly.

[25] report the following typical parameter values for CO₂ sequestration: $\mu = 5 \times 10^{-4}$ Pa s, $\phi = 0.2$, $\Delta \rho = 10$ kg m⁻³, $g = 9.81$ m s⁻², $D = 10^{-9}$ m² s⁻¹, and $10^{-14} \leq K \leq 10^{-12}$ m². Using these values,

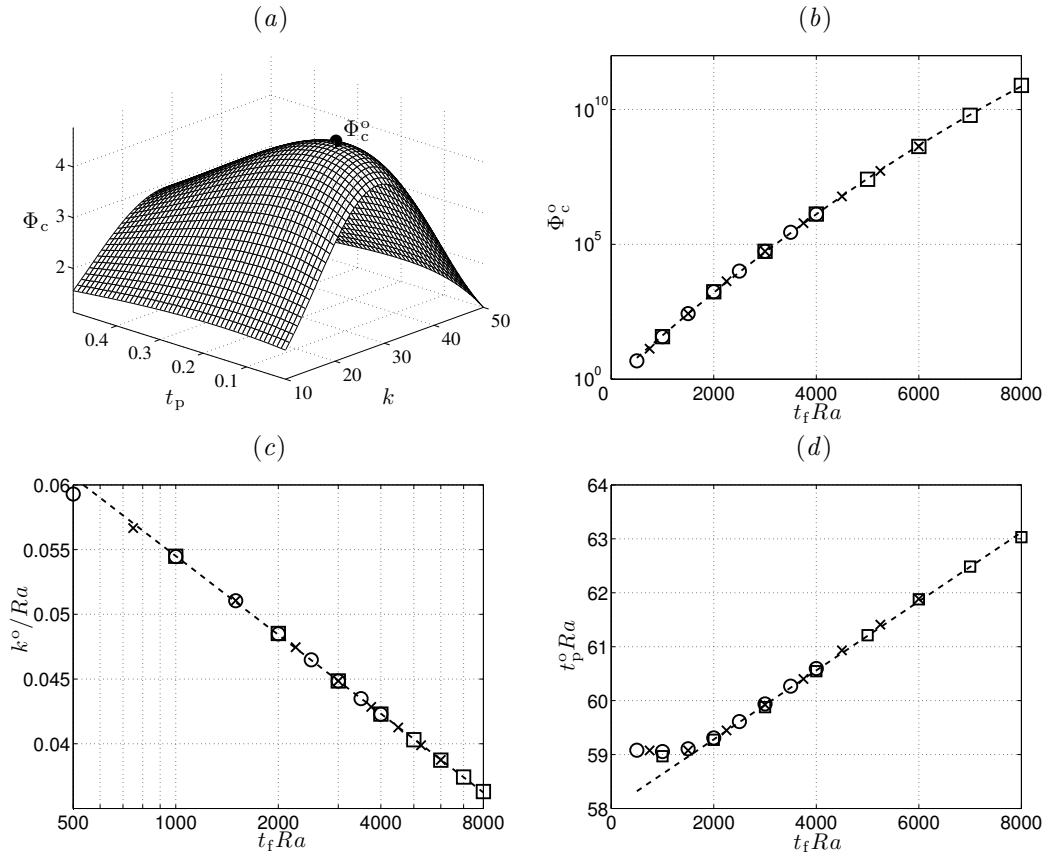


Figure 6: The optimal point (Φ_c^o, k^o, t_p^o) as a function of t_f and Ra . (a) Φ_c vs. t_p and k for $Ra = 500$ and $t_f = 1$. The solid dot marks (Φ_c^o, k^o, t_p^o) . (b) Φ_c^o vs. $t_f Ra$ for $Ra = 500$ (circles), $Ra = 750$ (crosses), and $Ra = 1000$ (squares). The dashed line shows relationship (24). (c) k^o/Ra vs. $t_f Ra$ for $Ra = 500$ (circles), $Ra = 750$ (crosses), and $Ra = 1000$ (squares). The dashed line shows relationship (25) (d) $t_p^o Ra$ vs. $t_f Ra$ for $Ra = 500$ (circles), $Ra = 750$ (crosses), and $Ra = 1000$ (squares). The dashed line shows relationship (26).

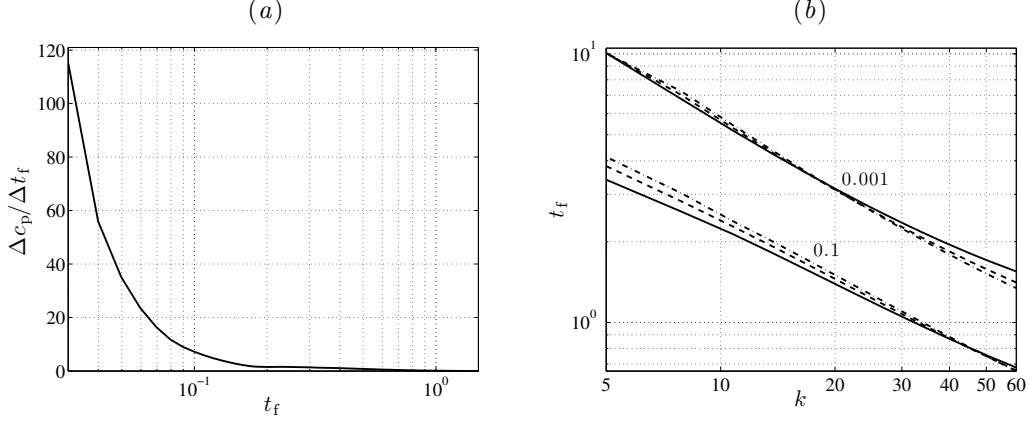


Figure 7: Convergence of the optimal c_p profiles for $t_p = 0.01$. (a) $\Delta c_p/\Delta t_f$ vs. t_f for $k = 30$ and $Ra = 500$ (b) Isocontours of $\Delta c_p/\Delta t_f$ in the (k, t_f) plane for $Ra = 500$ (solid line), $Ra = 750$ (dashed line), and $Ra = 1000$ (dash-dotted line).

figure 6 predicts that the optimal wavelength and initial time for high permeability aquifers, $K = 10^{-12}$ m², vary in the range, $11 \text{ cm} \leq 2\pi/k^* \leq 18 \text{ cm}$ and $17 \text{ hours} \leq t_p^* \leq 18 \text{ hours}$ as the final time varies between, $6 \text{ days} \leq t_f^* \leq 96 \text{ days}$. For low permeability aquifers, $K = 10^{-14}$ m², these parameters vary between $11 \text{ m} \leq 2\pi/k^* \leq 18 \text{ m}$, $19 \text{ years} \leq t_p^* \leq 21 \text{ years}$, $165 \text{ years} \leq t_f^* \leq 2636 \text{ years}$. While these initial and final times for $K = 10^{-14}$ m² aquifers may appear late, the optimal initial times are consistent with previous estimates of the critical time reported by [25] and [5]. Furthermore, in §6.2, we confirm that the range of final times are representative of actual onset times for nonlinear convection, t_o .

The dependence of the optimal point (k^o, t_p^o) on t_f indicates that the optimal initial perturbation depends on the initial perturbation amplitude and consequently cannot be determined through purely linear analysis. Consider, for example, that direct numerical simulations show that the onset time for convection, t_o , decreases with increasing initial perturbation amplitude [7, 8]. Consequently, figures 6(c) and 6(d) predict that large amplitude perturbations will have larger values of k^o and smaller values of t_p^o than small amplitude perturbations. Their exact values, however, would require *a priori* numerical or experimental results for the onset time t_o .

4.4 Influence of final time on initial perturbation profiles

We observe that beyond a certain final time, the initial profiles, c_p and w_p , are unaffected by further increases to t_f . To quantify the final time beyond which c_p and w_p do not depend on t_f , we measure the rate of change of c_p with respect to t_f as,

$$\frac{\Delta c_p}{\Delta t_f} = \frac{\|c_p(z; t_f + \Delta t_f) - c_p(z; t_f)\|_\infty}{\Delta t_f}, \quad (29)$$

where $\Delta t_f = 0.01$ and the c_p profiles are normalized with respect to their L^2 norms. Figure 7(a) illustrates $\Delta c_p/\Delta t_f$ versus t_f for $t_p = 0.01$, $k = 30$ and $Ra = 500$. We observe that $\Delta c_p/\Delta t_f$ is initially large but decreases rapidly to zero. Figure 7(b) illustrates isocontours of $\Delta c_p/\Delta t_f = 0.1$ and 0.001 in the (k, t_f) parameter plane for $t_p = 0.01$ and $Ra = 500$ (solid line), $Ra = 750$ (dashed line), and $Ra = 1000$ (dash-dotted line). With increasing k , the final time after which c_p and w_p do not change decreases. We observe only a small influence of the Rayleigh number on the $\Delta c_p/\Delta t_f$ isocontours.

The convergence of c_p and w_p beyond a certain t_f may be explained by noting that the forward IVP (5)–(7) always converges to the same dominant perturbations given sufficient time. To demonstrate this behavior, figure 8(a) illustrates random initial conditions for c_p (dashed line) and w_p (dash-dotted line) that span the entire vertical domain, $0 \leq z \leq 1$, at $t_p = 0.01$ for $k = 30$. Figure 8(b) illustrates the resulting perturbation profiles, $\hat{c}(z, 5)$ and $\hat{w}(z, 5)$, generated by integrating the forward IVP to $t = 5$.

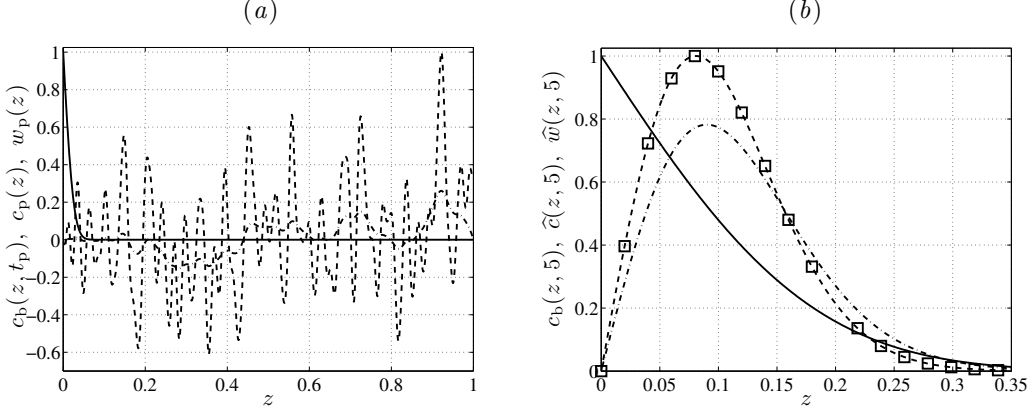


Figure 8: IVP results using random initial profiles, c_p and w_p , for $t_p = 0.01$, $k = 30$, and $Ra = 500$. (a) The base-state (solid line) and random initial profiles c_p (dashed line) and w_p (dash-dotted line) at $t_p = 0.01$. (b) Resulting perturbation profiles \hat{c} (dashed line) and \hat{w} (dash-dotted line) at $t = 5$. The squares show the corresponding optimal perturbation \hat{c} when $t_f = 5$.

The final state of the forward IVP is identical to the corresponding optimal perturbation, shown using squares in figure 8(b).

4.5 Comparison with QSSA modal analysis

The convergence of the forward IVP and optimization procedure to identical dominant perturbations at late times may be explained by considering a quasi-steady modal analysis. For a prescribed final time t_f , this approach approximates the base-state, $c_b(z, t)$, as steady and decomposes perturbations into separable functions of z and t ,

$$\hat{c} = c_e(z; t_f)e^{\sigma(t_f)t}, \quad \hat{w} = w_e(z; t_f)e^{\sigma(t_f)t}, \quad (30)$$

where $\sigma(t_f)$ is the instantaneous growth rate at $t = t_f$. Substituting (30) into (5)–(6) produces an eigenvalue problem for eigenvalues σ and eigenfunctions c_e and w_e . We compare the optimal perturbations with the dominant QSSA modes by measuring,

$$\Delta\hat{c} = \int_0^1 \left| \frac{c_e(z; t_f)}{\|c_e(z; t_f)\|_\infty} - \frac{\hat{c}(z, t_f)}{\|\hat{c}(z, t_f)\|_\infty} \right| dz. \quad (31)$$

When $\Delta\hat{c} = 0$, the dominant QSSA mode and optimal perturbation are identical.

Figure 9 compares optimal perturbations with dominant QSSA modes for $t_p = 0.1$ and $Ra = 500$. Note that t_p is chosen to be close to the optimal initial time t_p^o . Figure 9(a) illustrates the variation of $\Delta\hat{c}$ for wavenumbers $5 \leq k \leq 60$ and final times $0.12 \leq t_f \leq 2$. We observe large values of $\Delta\hat{c}$ at small wavenumbers and final times. In the limit of $k \rightarrow 0$, however, $\Delta\hat{c}$ tends to zero because the optimal perturbation and dominant QSSA mode both tend to $\hat{c} = \sin(\pi z/2) \exp(-\pi^2 Ra^{-1}t/4)$, see discussion of equation (22) in §4.2. With increasing wavenumber and final time, $\Delta\hat{c}$ becomes small, indicating that the optimal perturbations essentially recover the dominant QSSA modes. This behavior is confirmed in figure 9(b) which illustrates the base-state (solid line), optimal perturbation (dashed line), and dominant QSSA eigenmode (dash-dotted line) at $t_f = 2$ and $k = 10$. Note that $\Delta\hat{c}$ remains small for the optimal perturbations with wavenumber, k_{\max} , illustrated in figure 5(a).

The amplification produced by temporal integration of the dominant QSSA growth rate, σ , can be computed through the relation

$$\Phi_q(t) = e^{g(t)}, \quad g(t) = \int_{t_p}^t \sigma(t_f) dt_f. \quad (32)$$

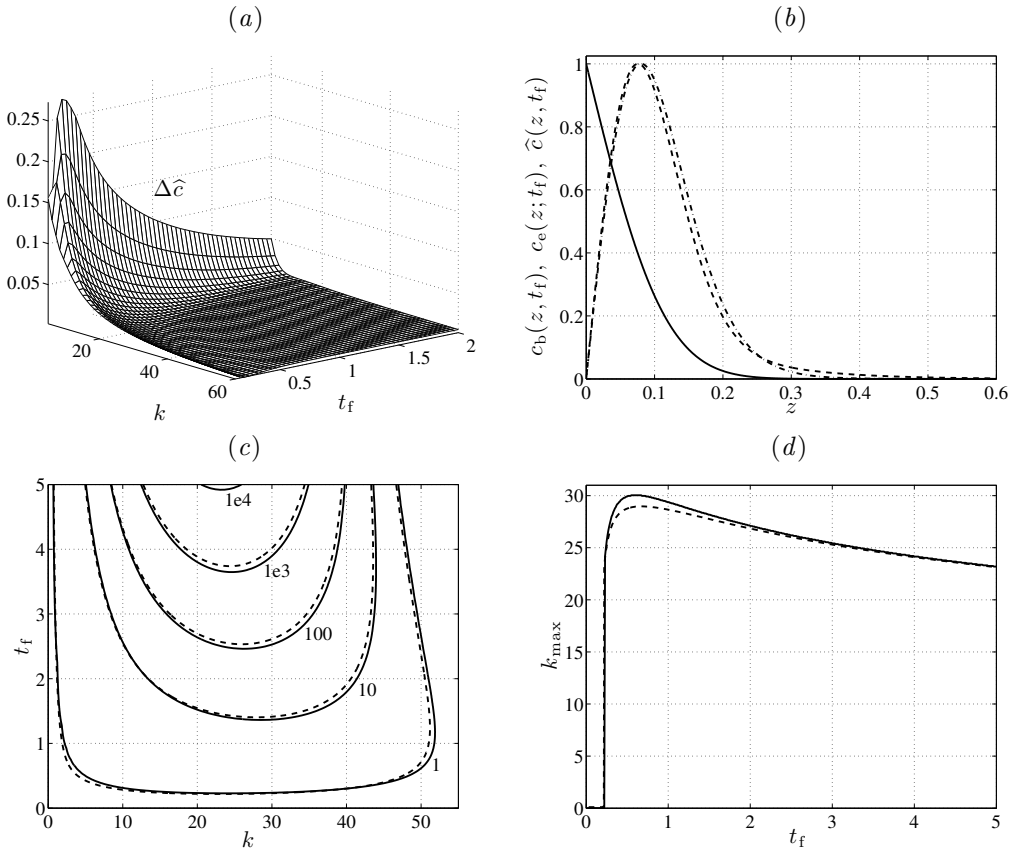


Figure 9: Comparison of optimal perturbations with the least stable QSSA mode for $Ra = 500$. (a) $\Delta \hat{c}$ in the (k, t_f) plane for $t_p = 0.1$. (b) illustrates base-state, $c_b(z, t_f)$ (solid line), optimal perturbation $\hat{c}(z, t_f)$ (dashed line) and least stable eigenmode, $c_e(z, t_f)$ (dash-dotted line) at t_f for $t_p = 0.1$, $k = 10$, and $t_f = 2$. (c) Isocontours of amplification in the (k, t_f) plane when $t_p = 0.01$ for QSSA (solid lines) and optimization (dashed lines). (d) The dominant wavenumbers k_{\max} vs. t_f when $t_p = 0.01$ for QSSA (solid lines) and optimization (dashed lines)

$t_p = 0.01$		$t_p = 0.1$		$t_p = 1$	
A_∞	$c_{\text{net}}^{\text{min}}$	A_∞	$c_{\text{net}}^{\text{min}}$	A_∞	$c_{\text{net}}^{\text{min}}$
10^{-02}	-10^{-02}	10^{-02}	-8.0×10^{-03}	10^{-02}	-2.1×10^{-03}
10^{-05}	-10^{-05}	10^{-05}	-4.9×10^{-06}	10^{-05}	-3.3×10^{-08}
10^{-10}	-10^{-10}	10^{-10}	-2.5×10^{-11}	10^{-10}	-5.1×10^{-15}

Table 1: Minimum net concentrations $c_{\text{net}}^{\text{min}}$ produced by the classical optimal c_p profiles when $k = 30$, $Ra = 500$, $t_f = 5$, $t_p = 0.01, 0.1, 1$, and $A_\infty = 10^{-2}, 10^{-5}$, and 10^{-10} . At $t_p = 0.01$, the negative concentration is of the same order as A_∞ . As t_p increases, the perturbation profiles become increasingly concentrated within the boundary layer and consequently the magnitude of the negative concentrations $c_{\text{net}}^{\text{min}}$ diminish.

Figure 9(c) compares isocontours of Φ_q (solid line) with optimal results for Φ_c (dashed line) in the (k, t_f) parameter plane for $Ra = 500$ and $t_p = 0.01$. We observe excellent agreement between the amplifications produced by optimal perturbations and dominant QSSA eigenmodes. Counterintuitively, for much of the (k, t_f) plane, Φ_q is marginally greater than Φ_c . This occurs for the following reasons. At late times, the boundary layer grows slowly and the optimal perturbations tend to the dominant QSSA eigenmodes. At small times, however, the boundary layer varies rapidly and the optimal perturbations cannot continuously adhere to the quasi-steady eigenmodes. Consequently, temporal integration of the dominant QSSA growth rates produces marginally larger amplifications than Φ_c . This also helps explain why dominant perturbations tend to differ from the dominant eigenmode at small times.

Figure 9(d) illustrates the dominant wavenumbers, k_{max} , that maximize Φ_q (solid line) and Φ_c (dashed line) for $0.03 \leq t_f \leq 5$. We repeat the optimization procedure for different t_p and observe similar agreement between the QSSA and optimization results. This suggests that optimal perturbations are primarily composed of the dominant QSSA mode. In contrast, nonmodal stability analyses of steady wall-bounded shear flows, such as channel flows and flat plate boundary layers, typically produce optimal perturbations that are qualitatively very different from the corresponding dominant eigenmodes. This suggests that for the current study, the deviation of the optimal perturbations from the dominant eigenmodes at small times is primarily due to the transient base-state, rather than the nonorthogonality of the quasi-steady eigenmodes.

5 Modified Optimization Procedure

Experimental studies observe that perturbations are initially localized within the boundary layer [27, 1, 9, 28, 3]. To determine whether the optimal perturbations obtained in §4 reflect those observed experimentally, we consider the following argument. If the optimal perturbation is observed experimentally, the net concentration can be expressed as the sum of the base-state and perturbation through the relation

$$c_{\text{net}}(x, z, t_p) = c_b(z, t_p) + A_\infty \cos(kx) \frac{c_p(z)}{\|c_p\|_\infty}, \quad (33)$$

where c_p is the optimal initial profile and A_∞ is the perturbation amplitude measured using the L^∞ norm. Table 1 lists the minimum net concentrations, $c_{\text{net}}^{\text{min}}$, for various A_∞ and t_p when $t_f = 5$, $k = 30$, and $Ra = 500$. For $t_p = 0.01$, we observe unphysical negative net concentrations equal to A_∞ . This occurs because the maxima of the optimal c_p profiles are located outside the boundary layer, see figure 5(b). For $t_p = 0.1$ and 1, the magnitude of the negative concentrations become increasingly smaller because the optimal c_p profiles become increasingly concentrated within the boundary layer, see figures 5(c)–5(d).

Direct numerical simulations show that the onset time for convection decreases with increasing initial perturbation amplitude A_∞ [8]. Consequently, though the classical optimal perturbations are mathematically valid optimal solutions, onset of convection in physical systems may more likely be triggered by suboptimal perturbations concentrated within boundary layer. Those perturbations support finite initial amplitudes, and consequently require less time to grow sufficiently for onset of convection. To investigate

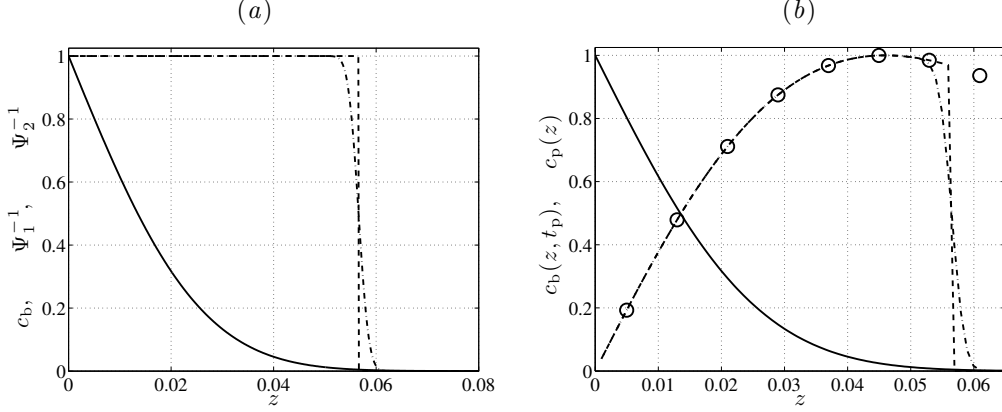


Figure 10: Optimization using Ψ_1 and Ψ_2 for $k = 30$, $Ra = 500$, $t_p = 0.1$, and $t_f = 3$. (a) Base-state (solid line), Ψ_1^{-1} (dashed line), and Ψ_2^{-1} (dash-dotted line). (b) Base-state (solid line), classical c_p (circles), and modified c_p profiles using Ψ_1 (dashed line) and Ψ_2 (dash-dotted line).

this alternate path to onset of convection, we propose a modified optimization procedure that constrains the initial concentration fields of the perturbations to be within the boundary layer.

5.1 Methodology

The classical optimization procedure described in §3 is modified by replacing the constraint $E(t_p) = 1$ with the modified constraint $E_\Psi(t_p) = 1$, where

$$E_\Psi(t_p) = \int_0^1 \Psi(z) \hat{c}(z, t_p)^2 dz, \quad (34)$$

where $\Psi(z)$ is a filter function that tends to infinity, $\Psi \rightarrow \infty$, outside the boundary layer. We then maximize $\Phi_\Psi = \sqrt{E(t_f)/E_\Psi(t_p)}$. The filter function assures that $E_\Psi(t_p) = \infty$, when c_p extends beyond the boundary layer. This forces Φ_Ψ to zero and effectively filters such perturbations from the optimization procedure. In practice, the infinite values of Ψ are approximated numerically using a large finite value.

Following an analogous procedure to that in §3, we formulate the Lagrangian,

$$\begin{aligned} \mathcal{L}(\hat{c}, c^*, \hat{w}, w^*, s) &= E(t_f) - s[E_\Psi(t_p) - 1] - \int_{t_p}^{t_f} \int_0^1 w^* (\mathcal{D}\hat{w} + k^2\hat{c}) dz dt \\ &\quad - \int_{t_p}^{t_f} \int_0^1 c^* \left(\frac{\partial \hat{c}}{\partial t} - \frac{1}{Ra} \mathcal{D}\hat{c} + \hat{w} \frac{\partial c_b}{\partial z} \right) dz dt, \end{aligned} \quad (35)$$

and obtain the following coupling conditions between physical and adjoint variables,

$$2s\hat{c}|_{t_p} = \Psi^{-1}c^*|_{t_p}, \quad 2\hat{c}|_{t_f} = c^*|_{t_f}. \quad (36)$$

The adjoint IVP (12)–(13) remains unchanged. After convergence of the iterative procedure for the optimal profile that maximizes Φ_Ψ , we compute the final amplification using the traditional definition of $\Phi_c = \sqrt{E(t_f)/E(t_p)}$. This allows us to compare results of the modified optimization procedure with those of the classical procedure.

5.2 Filter Functions

We first consider a filter function whose inverse is a step function of the form,

$$\Psi_1^{-1}(z) = \begin{cases} 1 & \text{if } z \leq \delta, \\ 0 & \text{if } \delta < z \leq 1, \end{cases} \quad (37)$$

where δ is the boundary layer depth defined as $c_b(\delta, t_p) = 0.005$. Figure 10(a) illustrates Ψ_1^{-1} as a dashed line for $t_p = 0.1$ and $Ra = 500$. The base-state is shown as a solid line. Figure 10(b) illustrates the corresponding optimal c_p profile (dashed line) for $Ra = 500$, $k = 30$, $t_p = 0.1$, and $t_f = 3$. The base-state is shown as a solid line and the classical optimal c_p profile is shown using circles. Within the boundary layer, the modified profile follows the classical profile and then vanishes discontinuously at $z = \delta$. Consequently, though concentrated within the boundary layer, the perturbations generated by Ψ_1 are unlikely to arise in nature.

To produce continuously differentiable perturbations, we introduce the following filter function that is equal to unity in most of the boundary layer, but varies smoothly to zero beyond the boundary layer depth,

$$\Psi_2^{-1}(z) = \frac{1}{2} \operatorname{erfc} \left(\frac{25(z - \delta)}{\delta} \right). \quad (38)$$

Figure 10(a) illustrates Ψ_2^{-1} using a dash-dotted line. Figure 10(b) illustrates that the corresponding optimal modified c_p profile (dash-dotted line) decreases rapidly, but smoothly, to zero outside the boundary layer, but is otherwise similar to that produced by Ψ_1 . The modified profiles illustrated in figure 10(b) produce physical initial conditions, $c_{\text{net}}^{\text{min}} = 0$, when $A_\infty < 10^{-3}$.

Though Ψ_2 produces physically realizable optimal perturbations, the perturbations have maxima near the boundary layer depth, $z = \delta$, where the base-state concentration is very small. This limits the maximum allowable initial amplitude of these perturbations. In contrast, perturbations with maxima near $z = 0$ can support larger initial amplitudes and may consequently trigger onset of convection sooner. Furthermore, one may expect that perturbations would naturally tend to have maxima near the upper boundary, $z = 0$, where the base-state has a maximum and there is consequently more solute to perturb. To investigate this possibility, we first note that the inverse filter functions may be interpreted as weight functions. Because Ψ_1^{-1} and Ψ_2^{-1} are equal to unity in most of the boundary layer, they give equal weight to most of the boundary layer. Optimal perturbations with maxima near $z = 0$ can be obtained using an inverse filter function that decreases with the base-state concentration. A natural candidate is $\Psi_3^{-1} = c_b$ because this naturally weighs regions of high base-state concentration over those with low base-state concentration.

Figure 11(a) illustrates the base-state (solid line) and c_p profile generated using Ψ_3 (dashed line) for $t_p = 0.1$, $t_f = 5$, $k = 30$, and $Ra = 500$. As expected, Ψ_3 produces a profile with a maximum closer to $z = 0$ than $z = \delta$. Consequently, the profile shown in figure 11(a) supports initial amplitudes as large as $A_\infty = 10^{-1}$ without producing negative values of c_{net} . Figure 11(b) illustrates optimal isocontours of Φ_c in the (k, t_f) parameter plane using Ψ_2 (solid lines) and Ψ_3 (dashed lines). As expected, though Ψ_3 supports larger initial amplitudes, Ψ_2 produces greater amplifications. This raises the possibility that there exists an optimal filter function, Ψ_{opt} , that balances the tradeoff between the initial amplitude and subsequent amplification in order to minimize the onset time for convection. This is beyond the scope of the current study, however, because it requires a nonlinear analysis. Therefore, for brevity, we focus on the perturbations produced by Ψ_3 because these support large initial amplitudes.

5.3 Comparison with classical optimization scheme

Hereinafter, we refer to the classical optimization procedure as COP and the modified optimization procedure using Ψ_3 as MOP. Figure 12(a) illustrates the temporal evolution of the dominant wavenumbers, k_{max} , produced by the COP (solid line) and MOP (dashed line) schemes for $t_p = 0.01$ and $Ra = 500$. For early final times, $t_f < 0.21$, the MOP scheme produces nonzero dominant wavenumbers, $k_{\text{max}} \neq 0$, while the COP scheme predicts $k_{\text{max}} = 0$. The large difference in dominant wavenumbers at small times occurs because the zero-wavenumber perturbations produced by the COP scheme span the entire vertical domain, $\hat{c} = \sin(\pi z/2) \exp(-\pi^2 Ra^{-1} t/4)$, as discussed in §4.2. Using the MOP scheme, these perturbations are filtered by Ψ_3 . At late t_f , the MOP dominant wavenumbers tend towards those predicted by the COP. Figure 12(b) illustrates the corresponding maximum amplifications, Φ_{max} , see equation (21), produced by the COP (solid line) and MOP (dashed line) schemes. For final times, $t_f < 0.21$, the COP amplifications are close to unity because the zero-wavenumber perturbations have a small constant decay rate, see discussion in §4.2. The MOP amplifications are an order-of-magnitude smaller because the perturbations are constrained to the boundary layer and undergo substantial damping up to the critical

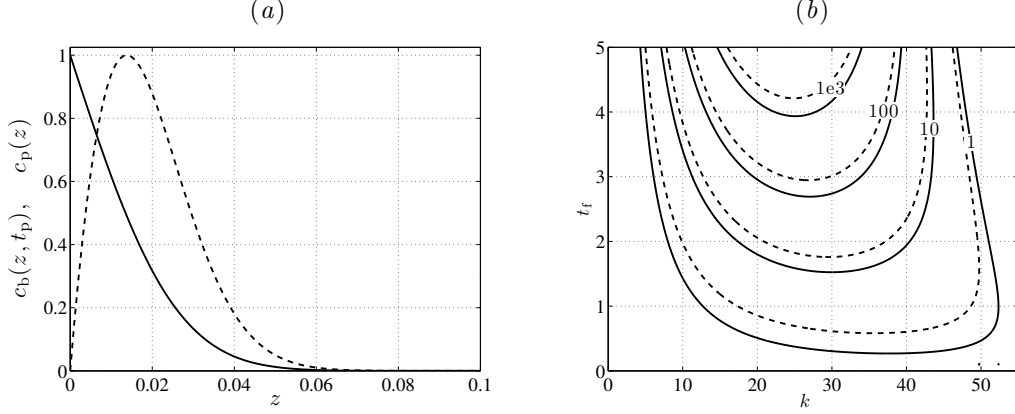


Figure 11: Optimization results for $t_p = 0.01$ and $Ra = 500$. (a) The base-state $c_b(z, t_p)$ (solid line) and optimal $c_p(z)$ profile using Ψ_3 (dashed line) for $t_f = 5$ and $k = 30$. Note that the initial $c_p(z)$ profile obtained using Ψ_2 is shown in figure 10(b). (b) Isocontours of Φ_c in (k, t_f) plane using Ψ_2 (solid line) and Ψ_3 (dashed line).

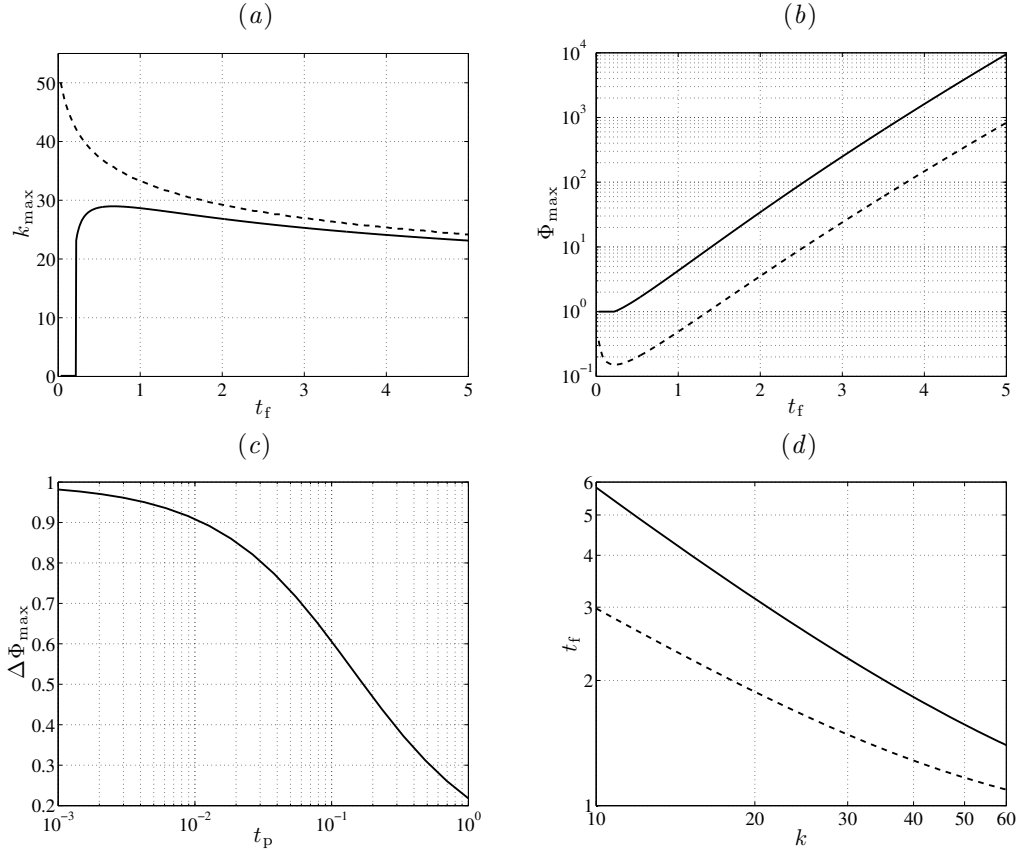


Figure 12: Comparison of the COP and MOP schemes for $Ra = 500$. (a) k_{\max} vs. t_f for $t_p = 0.01$ for COP (solid line) and MOP (dashed line). (b) Φ_{\max} vs. t_f for $t_p = 0.01$ for COP (solid line) and MOP (dashed line). (c) $\Delta\Phi_{\max}$ vs. t_p for $t_f = 4$. (d) Isocontours of $\Delta c_p / \Delta t_f = 0.001$ in the (k, t_f) plane for $t_p = 0.1$ for COP (solid line) and MOP (dashed line).

time for instability, t_c . For $t_f > 1$, the amplifications produced by COP and MOP in figure 12(b) have identical slopes. This occurs because of similar growth rates between the final states of the dominant wavenumber perturbations obtained using the COP and MOP schemes.

The difference between the COP and MOP amplifications depends on the initial time, t_p . To explore this, we measure

$$\Delta\Phi_{\max} = \frac{\Phi_{\text{COP}} - \Phi_{\text{MOP}}}{\Phi_{\text{COP}}}, \quad (39)$$

where Φ_{COP} and Φ_{MOP} are the maximum amplifications, Φ_{\max} , obtained using COP and MOP, respectively. Figure 12(c) illustrates $\Delta\Phi_{\max}$ for $t_f = 4$ as the initial perturbation time varies from $t_p = 10^{-3}$ to $t_p = 1$. Note that the results are independent of final time t_f when $t_f > 1$. $\Delta\Phi_{\max}$ tends to a maximum as $t_p \rightarrow 0$ because $\Phi_{\text{MOP}} \rightarrow 0$, while Φ_{COP} converges to finite values, see figures 4(c)–4(d). With increasing t_p , $\Delta\Phi_{\max}$ decreases indicating better agreement between the COP and MOP amplifications. Note that the maxima of the optimal initial MOP profiles are always closer to the top boundary, $z = 0$, compared to the initial COP profiles.

Recall from §4.4, that beyond certain final times, the initial c_p profiles generated by the COP scheme are insensitive to further increases in t_f . To investigate this behavior for the MOP scheme, figure 12(d) illustrates the isocontours $\Delta c_p / \Delta t_f = 0.001$, see equation (29), in the (k, t_f) parameter plane generated using the COP (solid line) and MOP (dashed line) schemes for $t_p = 0.1$ and $Ra = 500$. The final times beyond which the initial MOP profiles do not change shape are much smaller than the COP profiles. This suggests that initial perturbations confined within the boundary layer rapidly converge to a common shape.

As discussed in §4.3, due to the transient growth of the base-state, there exists an optimal combination of initial time and wavenumber, t_p^o and k^o , that produces the subsequent optimal amplification Φ_c^o . Figure 13(a) illustrates the MOP amplifications, Φ_c , for $10 \leq k \leq 50$, $0.1 \leq t_p \leq 0.5$, $t_f = 1$, and $Ra = 500$. The solid dot marks the peak of the surface, Φ_c^o . Figure 13 demonstrates Φ_c^o (panel b), k^o/Ra (panel c), and $t_p^o Ra$ (panel d) as functions of $t_f Ra$. The results for different Ra collapse as previously demonstrated for the COP scheme in figure 6. We obtain the following relationships for Φ_c^o and the dimensional forms of wavenumber, k^* , and the initial time, t_p^* ,

$$\log \Phi_c^o = -5.550 \times 10^{-8} t_f^{*2} \left(\frac{U^2}{\phi^2 D} \right)^2 + 0.001785 t_f^* \frac{U^2}{\phi^2 D} - 0.3967, \quad (40)$$

$$k^* = \frac{U}{\phi D} \left[0.1234 - 0.02237 \log \left(\frac{t_f^* U^2}{\phi^2 D} \right) \right], \quad (41)$$

$$t_p^* = -5.107 \times 10^{-7} t_f^{*2} \frac{U^2}{\phi^2 D} + 0.01086 t_f^* + 120.1 \frac{\phi^2 D}{U^2}. \quad (42)$$

For high permeability aquifers, $K = 10^{-12} \text{ m}^2$ (see §4.3), figure 13 predicts that the optimal perturbation wavelength and initial perturbation time vary in the range, $10 \text{ cm} \leq 2\pi/k^* \leq 18 \text{ cm}$ and $36 \text{ hours} \leq t_p^* \leq 51 \text{ hours}$ as the final time varies between, $6 \text{ days} \leq t_f^* \leq 96 \text{ days}$. For low permeability aquifers, $K = 10^{-14} \text{ m}^2$, these parameters vary in the range $10 \text{ m} \leq 2\pi/k^* \leq 18 \text{ m}$, $41 \text{ years} \leq t_p^* \leq 58 \text{ years}$, $165 \text{ years} \leq t_f^* \leq 2636 \text{ years}$. The optimal amplifications, Φ_c^o , are approximately 50 % those produced by the COP scheme, see figure 6. We observe that k^o agrees closely with those produced, using the COP scheme. The optimal initial perturbation times, t_p^o , however, are roughly twice as large as those for the COP scheme due to the large initial damping periods experienced by the MOP perturbations. The optimal initial time, t_p^o , is also more sensitive to t_f than the COP scheme. Recall from §4.3, that the optimal initial perturbation time would require *a priori* knowledge of the onset time of convection, i.e. $t_f = t_o$. Because of the increased sensitivity of t_p^o to t_f , we expect the optimal MOP perturbations to be more sensitive to initial perturbation amplitude, A_∞ , than the COP perturbations.

5.4 Comparison with QSSA $_\xi$ eigenvalue and IVP problems

In this section, we compare the modified optimization procedure to previously published linear stability methods that ensure perturbations are localized within the boundary layer. The first approach approximates the vertical domain as semi-infinite. In this case there is a similarity solution for the base-state,

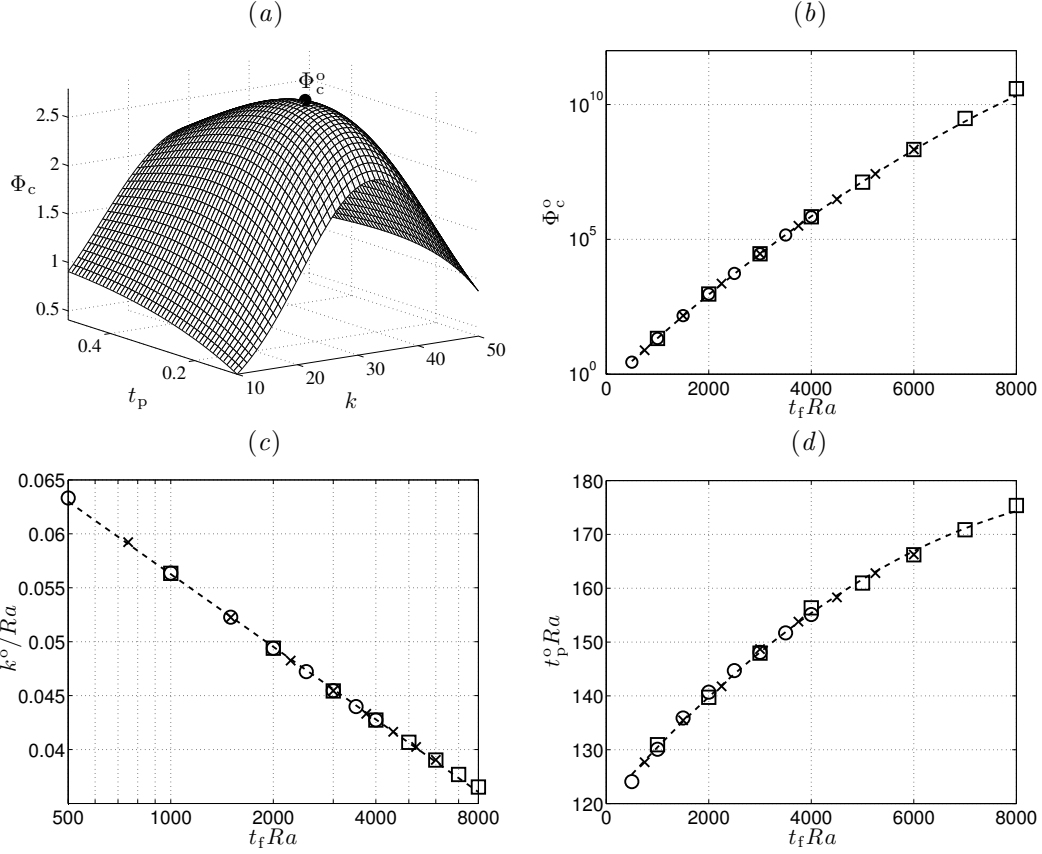


Figure 13: The optimal MOP point (Φ_c^o , k^o , t_p^o) as a function of t_f and Ra . (a) Φ_c vs. t_p and k for $Ra = 500$ and $t_f = 1$. The solid dot marks (Φ_c^o , k^o , t_p^o). (b) Φ_c^o vs. $t_f Ra$ for $Ra = 500$ (circles), $Ra = 750$ (crosses), and $Ra = 1000$ (squares). The dashed line shows relationship (40). (c) k^o/Ra vs. $t_f Ra$ for $Ra = 500$ (circles), $Ra = 750$ (crosses), and $Ra = 1000$ (squares). The dashed line shows relationship (41). (d) $t_p^o Ra$ vs. $t_f Ra$ for $Ra = 500$ (circles), $Ra = 750$ (crosses), and $Ra = 1000$ (squares). The dashed line shows relationship (42).

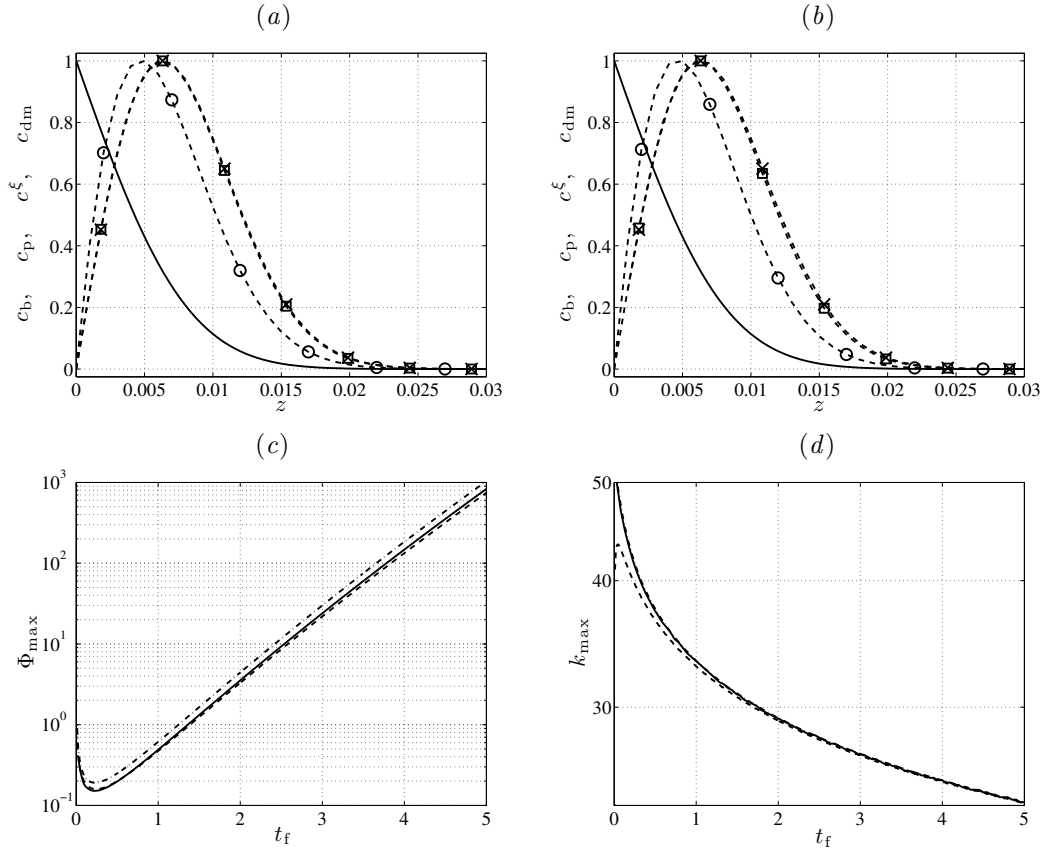


Figure 14: Comparison of modified optimization with QSSA in self-similar space and IVP with $c_p = c_{dm}$ for $Ra = 500$. (a) Base-state, c_b (solid line), initial MOP profile (circles), dominant QSSA $_{\xi}$ eigenmode, c^{ξ} (squares), and c_{dm} perturbation (43) (crosses) at $t_p = 0.01$ for $k = 10$. (b) Same as in panel (a) for $k = 50$. (c)–(d) Temporal evolution of Φ_{max} and k_{max} for $t_p = 0.01$ using MOP (solid line), QSSA $_{\xi}$ (dashed line), and initial condition (43) (dash-dotted line).

$c_b = 1 - \text{erf}(\xi)$, where $\xi(z, t) = z\sqrt{Ra/(4t)}$ is the similarity variable. [5] demonstrated that a quasi-steady modal analysis with respect to the (ξ, t) space produces eigenmodes concentrated in the boundary layer. For convenience of notation, we refer to this as the QSSA $_{\xi}$ problem. We refer to the eigenvectors of the QSSA $_{\xi}$ problem as c^{ξ} and w^{ξ} . The second procedure we consider is the solution of the forward IVP (5)–(7) using $c_p = c_{\text{dm}}$, where c_{dm} is the “dominant mode” of [5] given by,

$$c_{\text{dm}}(z) = \xi e^{-\xi^2}. \quad (43)$$

Initial condition (43) is the leading-order term of a Hermite polynomial expansion in the (ξ, t) space and has been used in numerous previous studies [29, 30, 5, 26, 31, 32, 11, 33].

Figure 14(a) illustrates the initial perturbation concentration profiles, $\widehat{c}(z, t_p)$, produced by the MOP (circles), dominant QSSA $_{\xi}$ eigenmode (squares), and initial condition (43) (crosses), for $t_p = 0.01$, $Ra = 500$, and $k = 10$. Figure 14(b) repeats figure 14(a) for the larger wavenumber, $k = 50$. In both figures, the base-state is shown as a solid line. For both wavenumbers, the three methodologies produce qualitatively similar profiles. The profiles produced by QSSA $_{\xi}$ and c_{dm} are indistinguishable, while the MOP profiles have maxima closer to $z = 0$. Note that the MOP profiles support slightly larger initial magnitudes, A_{∞} , than the QSSA $_{\xi}$ and c_{dm} profiles, without producing negative net concentrations, c_{net} .

Figure 14(c) illustrates results for Φ_{max} versus t_f obtained using the MOP (solid line), QSSA $_{\xi}$ (dashed line), and initial condition (43) for $t_p = 0.01$, $0.03 \leq t_f \leq 5$, and $Ra = 500$. The three procedures again produce similar results, though initial condition (43) produces marginally larger amplifications. Note that the QSSA $_{\xi}$ amplifications are obtained by first transforming the dominant QSSA $_{\xi}$ growth rates to the (z, t) coordinates using a L^2 norm, before integrating equation (32). Figure 14(d) illustrates the corresponding dominant wavenumbers, k_{max} , of the three procedures. The results produced by initial condition (43) and the MOP are indistinguishable.

6 Direct Numerical Simulations

We perform two-dimensional direct numerical simulations (DNS) of the nonlinear governing equations (1)–(2) using a traditional pseudospectral method with spectral spatial accuracy [34]. The horizontal domain is truncated to $x \in [0, L]$ with periodic boundary conditions on $x = 0$ and $x = L$. Equations (1)–(2) are then discretized spatially using Chebyshev polynomials in the vertical z direction and a Fourier expansion in the horizontal x direction. The advection-diffusion equation is discretized temporally using a third-order, semi-implicit, backwards-difference scheme [34]. This temporal discretization is chosen for its favorable stability and allows us to investigate small initial times, $t_p \rightarrow 0$, for which the DNS scheme of [8] was numerically unstable. The initial concentration field is prescribed at $t = t_p$ as

$$c_{\text{dns}}(z, x) = c_b(z) + A_{\infty} \frac{c_i(x, z)}{\|c_i\|_{\infty}}, \quad (44)$$

where A_{∞} is the initial perturbation magnitude measured with respect to the infinity norm of the perturbation concentration field, c_i .

6.1 DNS of physical systems

To emulate physical experiments, we perform DNS in which the boundary layer is simultaneously perturbed with all wavenumbers resolved numerically,

$$c_i(x, z) = \sum_{m=0}^{N/2-1} a_m \cos\left(\frac{2\pi m}{L} x\right) G(z) F(z), \quad (45)$$

where N is the number of collocation points in the x direction, and $-1 \leq F(z) \leq 1$ is a random function generated using Fortran’s random number generator. The coefficients a_m are computed to ensure that each horizontal Fourier mode is perturbed with equal energy. We set $L = 4\pi$ and $N = 1024$ in order to

Case	ζ_c	σ	Symbol
1	0.50	0.05	Circle
2	0.50	0.10	Square
3	0.50	0.15	Cross
4	0.25	0.10	Diamond
5	0.75	0.10	Plus

Table 2: The parameters used for the Gaussian, $G(z)$.

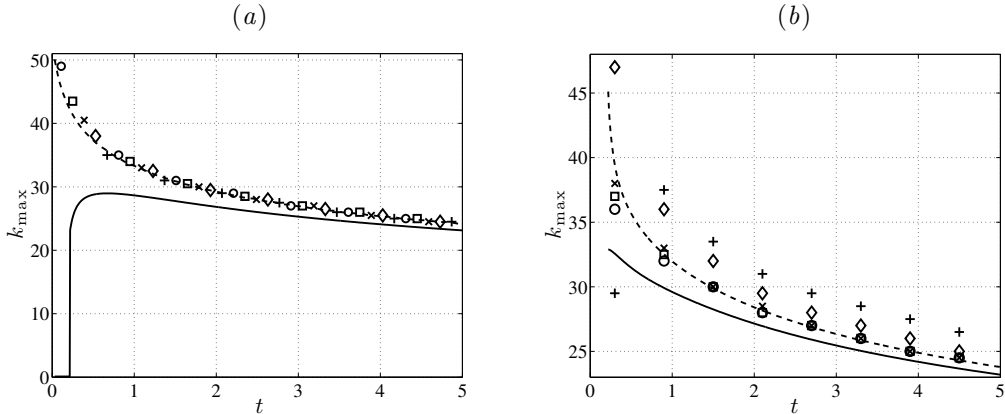


Figure 15: (a) Temporal evolution of dominant wavenumbers, k_{\max} , produced by DNS (symbols, see table 2), COP (solid line), and MOP (dashed line) for $Ra = 500$ and $t_p = 0.01$ (b) Same as in panel (a) for $t_p = 0.2$.

resolve wavenumbers, $k = 0, 0.5, 1, \dots, 255$. To ensure that c_i satisfies the boundary condition at $z = 0$ and remains concentrated within the boundary layer, we introduce the Gaussian function,

$$G(z) = \begin{cases} 0 & \text{if } z = 0, \\ \exp\left(-\frac{1}{2}\left(\frac{\zeta - \zeta_c}{\sigma}\right)^2\right) & \text{if } 0 < z \leq \delta, \\ 0 & \text{if } \delta < z \leq 1, \end{cases} \quad (46)$$

where $\zeta = z/\delta$, ζ_c is the mean and σ is the standard deviation. For example, when $\zeta_c = 0.5$, the peak of the Gaussian function is located midway between $z = 0$ and $z = \delta$. We vary the peak location, ζ_c , and the width, σ , to recreate several experimental possibilities listed in table 2.

Figure 15(a) illustrates the temporal evolution of the dominant wavenumbers, k_{\max} , produced by COP (solid line), MOP (dashed line), and five DNS recreating the experimental conditions in table 2, for $Ra = 500$ and $t_p = 0.01$. All simulations are run using the initial amplitude $A_\infty = 10^{-4}$ to produce a long linear regime, $t_o > 5$, to facilitate comparison of the dominant wavenumbers predicted by COP, MOP and DNS. We observe excellent agreement between the dominant wavenumbers produced by the MOP and DNS, while those predicted by the COP show poor agreement.

Figure 15(b) repeats figure 15(a) for the initial perturbation time $t_p = 0.2$, chosen to be near the optimal perturbation time, t_p^o . We first note that the DNS results for k_{\max} have a much wider spread than those for $t_p = 0.01$. This likely occurs because the initial damping period is much shorter for $t_p = 0.2$. Overall, we observe that MOP shows much better agreement with DNS than COP. For cases 1, 2, and 3 (see table 2) the agreement between MOP and DNS is excellent. For cases 4 and 5, MOP underpredicts k_{\max} , though it still outperforms COP. The improved agreement for cases 1, 2, and 3 may stem from the fact that the boundary layer was perturbed near $z = 0.5\delta$ in these cases. In cases 4 and 5, the layer was perturbed near $z = 0.25\delta$ and $z = 0.75\delta$, respectively.

Figure 16 illustrates the DNS result (circles) for the temporal amplification, Φ_c , of the $k = 30$ mode

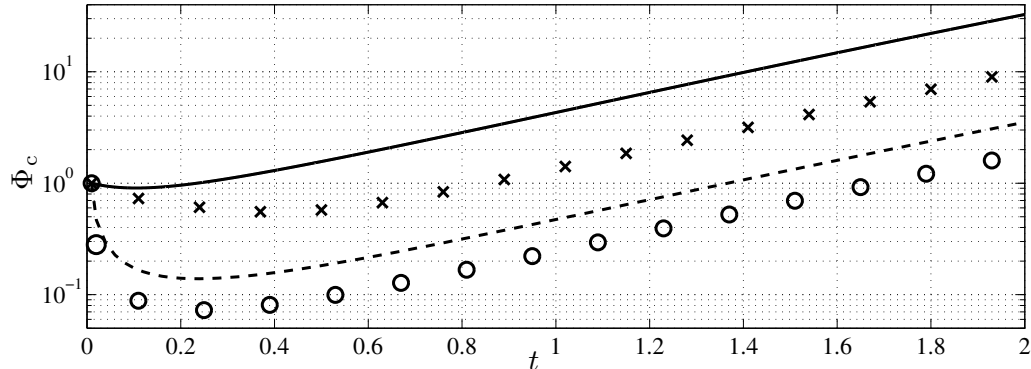


Figure 16: DNS result (circles) for the temporal amplification, Φ_c , of the $k = 30$ mode when the boundary layer is perturbed with initial condition (45) at $t_p = 0.01$ for case 1 (see table 2) and $Ra = 500$. For comparison, we also show the corresponding optimal amplifications produced by COP (solid line) and MOP (dashed line) for $k = 30$, $Ra = 500$, and $t_p = 0.01$. The crosses illustrate the amplifications produced when the forward IVP is integrated using the unphysical random initial condition illustrated in figure 8(a).

when the boundary layer is perturbed with initial condition (45) at $t_p = 0.01$ for case 1 (see table 2) and $Ra = 500$. For comparison, the figure also illustrates the corresponding optimal amplifications produced by COP (solid line) and MOP (dashed line) for $k = 30$, $Ra = 500$, and $t_p = 0.01$. As expected, the unphysical COP perturbation has the smallest initial damping period and largest amplifications because it is not constrained to the boundary layer region. The DNS and MOP perturbations both experience considerable damping; however, the DNS perturbation experiences greater damping because condition (45) initially excites heavily damped modes. Following the initial damping period, $t > 0.4$, the DNS, MOP, and COP perturbations experience identical growth rates such that the amplifications in figure 16 have identical slopes. Previously, [35] interpreted these identical slopes as confirmation of their nonmodal stability analysis. We find, however, that the identical slopes are due to the fact that all initial perturbations, optimal or suboptimal, rapidly converge to the dominant QSSA eigenmode (see §4.5). To illustrate this point, the crosses in figure 16 show the amplifications produced when the forward IVP is integrated for a random initial condition, illustrated in figure 8(a), that spans the entire domain. The random initial condition produces identical slopes for $t > 0.6$.

6.2 Extent of linear regime and onset of convection

We now demonstrate the existence of a well-defined linear regime preceding onset of convection, and we compare the onset times, t_o , produced by the MOP and COP schemes. We measure t_o for different values of A_∞ and t_p by specifying the following initial concentration field,

$$c_{\text{dns}}(x, z) = c_b(z) + A_\infty \cos(kx) \frac{c_p(z)}{\|c_p\|_\infty}, \quad (47)$$

where c_p are the optimal initial profiles determined by COP or MOP. Motivated by experiments [9, 23], we define t_o as the time at which $dJ/dt = 0$, where J is the mean flux of CO_2 into the brine given by,

$$J(t) = -\frac{1}{L} \int_0^L \frac{1}{Ra} \frac{\partial c_{\text{dns}}}{\partial z} \Big|_{z=0} dx. \quad (48)$$

Note from (48) that perturbations oscillating sinusoidally in the horizontal direction have no net effect on J . Consequently, during the linear regime, the net flux is due to pure diffusion of the base-state, i.e. $J = J_b$. The deviation of the DNS results for J from J_b is due to the growth of a zero-wavenumber

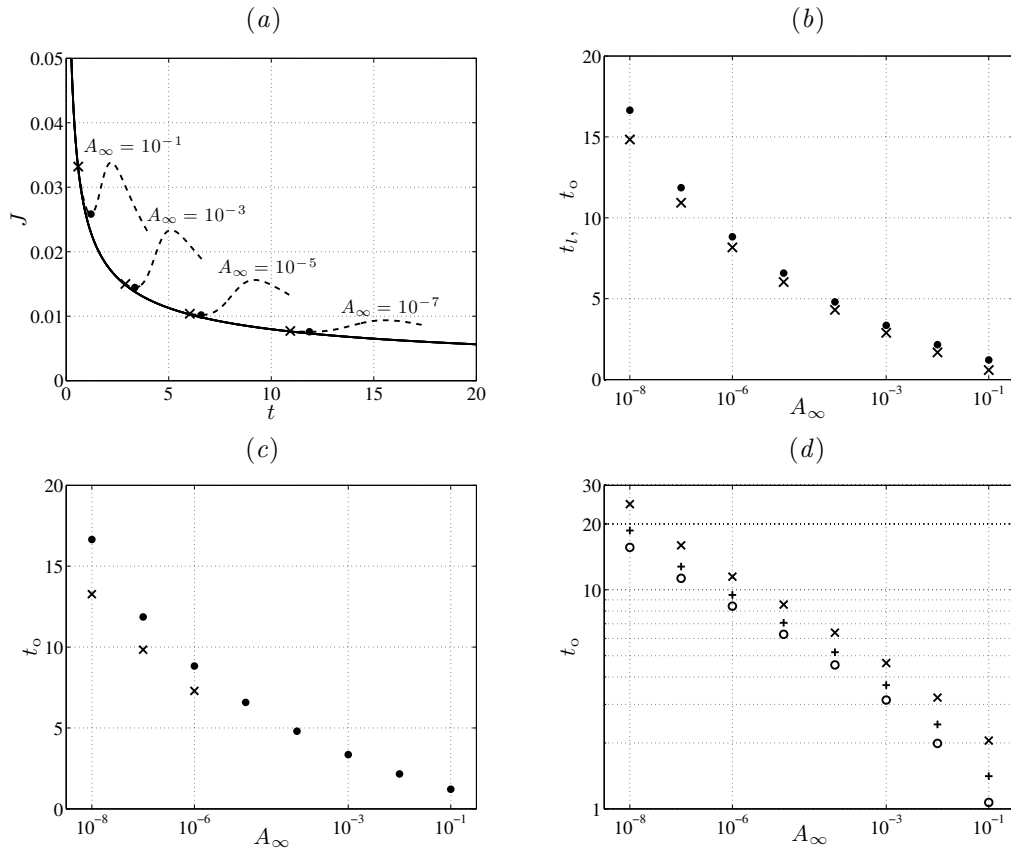


Figure 17: DNS results for $Ra = 500$ and $k = 30$ (a) the flux due to base-state, J_b (solid lines), and the flux from DNS, J , (dashed lines) using the MOP c_p profile at $t_p = 0.1$. The crosses denote t_l while the solid dots denote t_o . (b) t_l (crosses) and t_o (solid dots) vs. A_∞ using the MOP c_p profile at $t_p = 0.1$. (c) t_o vs. A_∞ using the COP (crosses) and MOP (solid dots) c_p profiles at $t_p = 0.1$. (d) t_o vs. A_∞ using the MOP c_p profiles at $t_p = 0.01$ (crosses), $t_p = 0.05$ (plus signs), and $t_p = 0.2$ (circles). Note that a log scale has been used for t_o .

mode, $k = 0$, due to nonlinear interactions [36]. To further quantify the duration of the linear regime, we also measure the time, $t = t_l$, for which $J/J_b = 1.01$.

Figure 17(a) presents DNS results for J using the optimal c_p profile produced by MOP for $t_p = 0.1$, $t_f = 5$, $k = 30$, and $Ra = 500$. Note that the MOP c_p profiles are insensitive to the final time when $t_f > 1$. The solid line shows the temporal evolution of the flux due to the base-state, J_b , while the dashed lines show DNS results for J when $A_\infty = 10^{-1}$, 10^{-3} , 10^{-5} , and 10^{-7} . The times, t_l and t_o , are marked with solid dots and crosses respectively. The flux J initially agrees with J_b and then deviates after $t = t_l$ due to nonlinear effects. The initial linear regime exists even in the case of large initial amplitude $A_\infty = 10^{-1}$. Figure 17(b) illustrates t_l (crosses) and t_o (solid dots) for various perturbation amplitudes A_∞ .

Figure 17(c) illustrates t_o versus A_∞ using the optimal profiles produced by COP (crosses) and MOP (solid dots) for $t_p = 0.1$, $t_f = 5$, $k = 30$, and $Ra = 500$. The COP scheme produces negative net concentration fields, c_{net} , for all finite perturbation amplitudes, see table 1. For illustration purposes, we arbitrarily set the maximum amplitude for COP to $A_\infty = 10^{-6}$ for which $c_{\text{net}}^{\text{min}} = -4.1 \times 10^{-7}$. In this case, COP produces onset times as low as $t_o = 7.29$ for $A_\infty = 10^{-6}$. We stress, however, that the onset times predicted by COP cannot be realized in physical systems because of $c_{\text{net}}^{\text{min}} < 0$, and are shown for illustration purposes only. In comparison, the MOP supports finite initial amplitudes as large as $A_\infty = 10^{-1}$ for which $t_o = 1.21$. We conclude that the perturbations produced by the MOP are more likely to trigger onset of convection in physical systems.

Figure 17(d) illustrates t_o versus A_∞ using the MOP c_p profiles at $t_p = 0.01$ (crosses), $t_p = 0.05$ (plus signs), and $t_p = 0.2$ (circles) for $t_f = 5$, $Ra = 500$, and $k = 30$. Onset of convection occurs later for smaller t_p due to the strong initial damping periods. Note that a log scale has also been used for t_o to highlight the difference for larger A_∞ . For large amplitude perturbations, we observe that onset of convection can occur around $t_o \approx 1$. For typical aquifer conditions (see §4.3), with permeability $K = 10^{-14} \text{ m}^2$ and height, $H = 51 \text{ m}$, this corresponds to a dimensional onset time of $t_o^* \approx 165 \text{ years}$.

7 Conclusions and summary

We investigated the linear stability of gravitationally unstable, transient, diffusive boundary layers in isotropic, homogeneous porous media. We began by performing a classical optimization procedure (COP) to determine optimal perturbations with maximum amplifications. Previous studies [16, 17] have observed that perturbation amplification is sensitive to the perturbation flow field used to measure perturbation magnitude. Because this sensitivity has not been addressed for applications to CO_2 sequestration, we compared three different measures of perturbation amplitude that maximize either the perturbation concentration field, vertical velocity field, or the sum of the perturbation velocity and concentration fields, which we refer to as the total energy. We determined that maximizing the perturbation concentration field naturally maximizes the total energy. Maximizing the perturbation velocity field, however, does so at the expense of the concentration field and total energy. Consequently, we focus our study on perturbations that maximize the concentration field because we expect these to be the dominant trigger for onset of nonlinear convection.

Due to the transient nature of the base-state, optimal perturbations are sensitive to the initial time, $t = t_p$, at which the boundary layer is perturbed. Moreover, for a given final time, $t = t_f$, there is a unique initial perturbation time, t_p^o , and wavenumber, k^o , that maximize perturbation growth. By rescaling the problem, we obtained approximate analytical relationships, see equations (24)–(26), for the optimal amplification, wavenumber, and initial perturbation time. These relationships show that t_p^o and k^o are independent of the aquifer height, H , but sensitive to the final time t_f . This indicates that the optimal initial perturbation depends on the onset time for nonlinear convection, t_o , and consequently the initial perturbation amplitude. Relationships (24)–(26) also predict that large amplitude perturbations with small onset times will have larger optimal wavenumbers, k^o , and smaller optimal initial perturbation times, t_p^o , than small amplitude perturbations with late onset times.

As the final time, t_f , increases, the optimal initial perturbations eventually converge to a fixed shape and cease to vary with increasing t_f . This occurs because the final perturbations at $t = t_f$ rapidly tend to the dominant quasi-steady eigenmode. In fact, we demonstrate that for the current problem, the quasi-steady modal analysis is a good approximation to the COP. Both methods produce nearly identical

amplifications and dominant wavenumbers. This suggests that the deviation of the optimal perturbations from the dominant eigenmodes at small times may be primarily due to the transient base-state, rather than the nonorthogonality of the quasi-steady eigenmodes. This is in stark contrast to wall-bounded shear flows for which non-orthogonal eigenmodes often play a dominant role.

To judge the relevance of optimal perturbations to physical systems, we demonstrate that every perturbation has a maximum allowable initial amplitude above which the sum of the base-state and perturbation produces unphysical negative concentrations. We demonstrate that the optimal initial perturbations predicted by the COP produce unphysical negative concentrations for all finite initial amplitudes. Consequently, onset of convection in physical systems is more likely triggered by suboptimal perturbations that support finite amplitudes. To explore this alternate path to onset of convection, we developed a modified optimization procedure (MOP) that constrains the initial perturbations to be concentrated within the boundary layer.

An integral characteristic of the MOP is the concept of a filter function, $\Psi(z)$, that effectively filters out perturbations with concentration fields extending beyond the boundary layer, see equation (34). The choice of filter function is not unique, and determines both the maximum allowable initial perturbation amplitude as well as the subsequent perturbation amplification. Filter functions that concentrate the initial perturbation close to $z = 0$ support large initial amplitudes, but produce small subsequent amplifications. Filter functions that concentrate the perturbations near the boundary layer depth support small initial amplitudes, but produce large subsequent amplifications. This raises the possibility that there exists an optimal filter function that balances the effects of the initial amplitude and subsequent amplification in order to minimize the onset time for convection. Because this requires a nonlinear analysis, we leave its consideration to future work. Rather, we focussed on perturbations produced by $\Psi = c_b^{-1}$ because this naturally concentrates perturbations in regions of large base-state concentration, and because it shows good agreement with corresponding DNS of physical systems.

The alternate path to onset of convection taken by the MOP features smaller amplifications and larger dominant wavenumbers than the COP, especially at small initial perturbation times, $t_p \ll t_p^o$. This occurs because the dominant MOP perturbations are concentrated within the boundary layer, and consequently experience more initial damping than the COP perturbations. We obtained approximate analytical relationships (40)–(42) for the optimal amplification, wavenumber, and initial perturbation time. The optimal initial times produced by the MOP are roughly twice those produced by the COP. We also observed that MOP perturbations are more sensitive to variations in t_f , and consequently more sensitive to the initial perturbation amplitude, than the COP perturbations. We demonstrated that the results produced by MOP agree well with the “dominant mode” approach of [5] as well as quasi-steady modal analyses performed in the similarity space of the base-state [5, 26, 31].

To emulate physical experiments, we performed DNS in which the boundary layer is simultaneously perturbed with all wavenumbers resolved by the simulations. The perturbations have a random structure but are concentrated within the boundary layer. The DNS results confirm that physical systems follow the alternate path to convection predicted by the MOP scheme and show poor agreement with COP. Furthermore, the MOP perturbations support large initial amplitudes, $A_\infty \sim 10^{-1}$, and produce early onset times for nonlinear convection. In contrast, the COP perturbations support neither finite amplitudes nor finite onset times. In an ongoing study, we are comprehensively exploring the effects of wavenumber, initial amplitude, initial time, and Rayleigh number on the onset of nonlinear convection. This is being performed using a weakly nonlinear expansion that is beyond the scope of the current study.

8 Acknowledgements

DD gratefully acknowledges all researchers in this field, without their tireless efforts, this research would not have come into fruition. DD also thanks co-authors NT and AR for guidance and inspiration that aided him in completing his PhD at the University of Maryland, College Park. This research was supported through a research grant from the Petroleum Institute, Abu Dhabi.

References

- [1] J. W. Elder. The unstable thermal interface. *J. Fluid Mech.*, 32(01):69–96, 1968.
- [2] A. W. Goldstein. Stability of a horizontal fluid layer with unsteady heating from below and time-dependent body force. Technical Report NASA-TR-R-4, NASA, 1959.
- [3] R. A. Wooding, S. W. Tyler, and I. White. Convection in groundwater below an evaporating salt lake: 1. Onset of instability. *Water Resour. Res.*, 33(6):1199–1217, 1997.
- [4] P. Drazin and W. Reid. *Hydrodynamic Stability*. Cambridge University Press, 1982.
- [5] A. Riaz, M. Hesse, H. A. Tchelepi, and F. M. Orr. Onset of convection in a gravitationally unstable diffusive boundary layer in porous media. *J. Fluid Mech.*, 548:87–111, 2006.
- [6] R. Farajzadeh, H. Salimi, P. L. J. Zitha, and H. Bruining. Numerical simulation of density-driven natural convection in porous media with application for CO₂ injection projects. *Int. J. Heat Mass Tran.*, 50:5054–5064, 2007.
- [7] A. Selim and D. A. S. Rees. The stability of developing thermal front in a porous medium. II. Nonlinear evolution. *J. Porous Media*, 10(1):17–34, 2007.
- [8] S. Rapaka, S. Chen, R. J. Pawar, P. H. Stauffer, and D. Zhang. Non-modal growth of perturbations in density-driven convection in porous media. *J. Fluid Mech.*, 609:285–303, 2008.
- [9] L. M. Blair and J. A. Quinn. The onset of cellular convection in a fluid layer with time-dependent density gradients. *J. Fluid Mech.*, 36(02):385–400, 1969.
- [10] D.A.S. Rees, A. Selim, and J.P. Ennis-King. The instability of unsteady boundary layers in porous media. In Peter Vadasz, editor, *Emerging Topics in Heat and Mass Transfer in Porous Media*, volume 22 of *Theory and Applications of Transport in Porous Media*, pages 85–110. Springer Netherlands, 2008.
- [11] M.C. Kim and C.K. Choi. Linear stability analysis on the onset of buoyancy-driven convection in liquid-saturated porous medium. *Phys. Fluids*, 24(4):044102, 2012.
- [12] P. J. Schmid. Nonmodal stability theory. *Annu. Rev. Fluid Mech.*, 39:129–162, 2007.
- [13] B. F. Farrell and P. J. Ioannou. Generalized stability theory. Part I: Autonomous operators. *J. Atmos. Sci.*, 53(14):2025–2040, 1996.
- [14] B. F. Farrell and P. J. Ioannou. Generalized stability theory. Part II: Nonautonomous operators. *J. Atmos. Sci.*, 53(14):2041–2053, 1996.
- [15] S. Whitaker. *The Method of Volume Averaging*. Kluwer Academic Publishers, 1999.
- [16] C. T. Tan and G. M. Homsy. Stability of miscible displacements in porous media: Rectilinear flow. *Phys. Fluids*, 29:3549–3556, 1986.
- [17] F. Doumenc, T. Boeck, B. Guerrier, and M. Rossi. Transient Rayleigh–Bénard–Marangoni convection due to evaporation: a linear non-normal stability analysis. *J. Fluid Mech.*, 648:521–539, 2010.
- [18] J.-P. Caltagirone. Stability of a saturated porous layer subject to a sudden rise in surface temperature: Comparison between the linear and energy methods. *Q. J. Mech. Appl. Math.*, 33(1):47–58, 1980.
- [19] J. Ennis-King, I. Preston, and L. Paterson. Onset of convection in anisotropic porous media subject to a rapid change in boundary conditions. *Phys. Fluids*, 17:Article no. 084107, 2003.
- [20] M.C. Kim and S. Kim. Onset of convective stability in a fluid-saturated porous layer subjected to time-dependent heating. *Int. Commun. Heat Mass*, 32:416 – 424, 2005.

- [21] T. D. Foster. Stability of a homogeneous fluid cooled uniformly from above. *Phys. Fluids*, 8(7):1249–1257, 1965.
- [22] P. M. Gresho and R. L. Sani. The stability of a fluid layer subjected to a step change in temperature: Transient vs. frozen time analyses. *Int. J. Heat Mass Tran.*, 14(2):207 – 221, 1971.
- [23] M. Kaviany. Onset of thermal convection in a saturated porous medium: experiment and analysis. *Int. J. Heat Mass Tran.*, 27(11):2101 – 2110, 1984.
- [24] A.C. Slim and T.S. Ramakrishnan. Onset and cessation of time-dependent, dissolution-driven convection in porous media. *Phys. Fluids*, 22(12):124103, 2010.
- [25] J. Ennis-King and L. Paterson. Role of convective mixing in the long-term storage of carbon dioxide in deep saline formations. *SPE J.*, 10:349–356, 2005.
- [26] A. Selim and D. A. S. Rees. The stability of developing thermal front in a porous medium. I. Linear theory. *J. Porous Media*, 10:1–16, 2007.
- [27] W. G. Spangenberg and W. R. Rowland. Convective circulation in water induced by evaporative cooling. *Phys. Fluids*, 4:743–750, June 1961.
- [28] L. L. Green and T. D. Foster. Secondary convection in a Hele Shaw cell. *J. Fluid Mech.*, 71(04):675–687, 1975.
- [29] Y. Ben, E. A. Demekhin, and H.-C Chang. A spectral theory for small-amplitude miscible fingering. *Phys. Fluids*, 14(3):999–1010, 2002.
- [30] D. Pritchard. The instability of thermal and fluid fronts during radial injection in a porous medium. *J. Fluid Mech.*, 508:133–163, 2004.
- [31] D. Wessel-Berg. On a linear stability problem related to underground CO₂ storage. *SIAM J. Appl. Math.*, 70(4):1219–1238, 2009.
- [32] M.C. Kim and C.K. Choi. The stability of miscible displacement in porous media: nonmonotonic viscosity profiles. *Phys. Fluids*, 23(8):084105, 2011.
- [33] M. T. Elenius, J. M. Nordbotten, and H. Kalisch. Effects of capillary transition on the stability of a diffusive boundary layer. *IMA J. Appl. Math.*, 77(6):771–787, 2012.
- [34] R. Peyret. *Spectral Methods for Incompressible Viscous Flows*. Springer-Verlag, New York, 2002.
- [35] S. Rapaka, R. J. Pawar, P. H. Stauffer, D. Zhang, and S. Chen. Onset of convection over a transient base-state in anisotropic and layered porous media. *J. Fluid Mech.*, 641:227–244, December 2009.
- [36] B. S. Jhaveri and G. M. Homsy. The onset of convection in fluid layers heated rapidly in a time-dependent manner. *J. Fluid Mech.*, 114:251–260, 1982.